UNIVERSITY OF SÃO PAULO
SÃO CARLOS SCHOOL OF ENGINEERING

Pedro Henrique Rosa dos Santos

Numerical simulation of the receptivity of Tollmien-Schlichting waves due to acoustic waves inciding on rectangular hump and gap in compressible flow

São Carlos

2022

Pedro Henrique Rosa dos Santos

Numerical simulation of the receptivity of Tollmien-Schlichting waves due to acoustic waves inciding on rectangular hump and gap in compressible flow

Dissertation presented to the São Carlos School of Engineering, University of São Paulo, Brazil, to obtain the degree of Master in Sciences - Graduate Program in Mechanical Engineering.

Concentration area: Aeronautics

Advisor: Marcello Augusto Faraco de Medeiros

CORRECTED VERSION

São Carlos

2022

FOLHA DE JULGAMENTO

Candidato: **PEDRO HENRIQUE ROSA DOS SANTOS**

Título da dissertação: "Simulação numérica da receptividade de ondas Tollmien-Schlichting devido à incidência de ondas acústicas em ressalto e cavidade retangulares em escoamento compressível"

Data da defesa: 07/12/2022

Comissão Julgadora   **Resultado**

Prof. Associado **Marcello Augusto Faraco de Medeiros**   **Aprovado**
(Orientador)
(Escola de Engenharia de São Carlos – EESC/USP)

Prof. Dr. **Marco Placidi**   **Aprovado**
(University of Surrey)

Prof. Dr. **Sávio Brochini Rodrigues**   **Aprovado**
(Universidade Federal de São Carlos – UFSCar)

Coordenador do Programa de Pós-Graduação em Engenharia Mecânica:
Prof. Associado **Adriano Almeida Gonçalves Siqueira**

Presidente da Comissão de Pós-Graduação:
Prof. Titular **Murilo Araujo Romero**

Dedico este trabalho a Deus, pois sem ele eu não teria capacidade para desenvolvê-lo. Dedico também à minha querida família, que tanto admiro, e em especial aos meus pais, a quem agradeço as bases que deram para me tornar a pessoa que sou hoje.

ACKNOWLEDGEMENTS

Primeiramente agradeço a Deus por me permitir ter a saúde e força de vontade para a realização deste trabalho.

À minha família, Edna, Maurílio, Júlia e Natália, por todo o apoio e pela ajuda, que muito contribuíram para a realização deste trabalho.

À minha noiva Débora Maria, que sempre esteve ao meu lado nos momentos mais difíceis.

Ao meu orientador, o Professor Dr. Marcello Augusto Faraco de Medeiros, por ter aceitado acompanhar-me neste projeto. O seu empenho foi essencial para a minha motivação à medida que as dificuldades iam surgindo ao longo do percurso.

Aos meus colegas de trabalho, pelo apoio incondicional durante a minha jornada.

Aos meus colegas da pós-graduação no Departamento de Engenharia Aeronáutica, pelo companheirismo e pela amizade.

Aos meus colegas de laboratório, Ana, Marlon, Fernando, Victor, Felipe, Giovanni, Christian e Matheus, pela troca de experiências que me permitiram crescer.

A todos os profissionais do departamento de Engenharia Mecânica da Universidade de São Paulo por todo o apoio que me deram ao longo do percurso, e por todas as bases acadêmicas e profissionais necessárias para a realização deste trabalho.

"Pois nada há de oculto que não venha a ser revelado, e nada em segredo que não seja trazido à luz do dia."

Mateus 4,22

RESUMO

DOS SANTOS, P. H. R. **Simulação numérica da receptividade de ondas Tollmien-Schlichting devido à incidência de ondas acústicas em ressalto e cavidade retangulares em escoamento compressível**. 2022. 76p. Dissertation (Master) - São Carlos School of Engineering, University of São Paulo, São Carlos, 2022.

A receptividade acústica das ondas TS devido à rugosidade localizada retangular (cavidade e ressalto) dentro de uma camada limite laminar compressível foi estudada. O método utilizado foi a Simulação Numérica Direta com diferenças finitas compactas de alta ordem e malha de ajuste ao corpo. O espaço paramétrico cobriu pequenas não uniformidades positivas ou negativas, e uma altura inicial de ressalto considerada não linear para receptividade. O espaço também inclui diferentes números de Mach.

Uma nova maneira de medir a receptividade foi sugerida. A comparação com os dados de simulação da literatura forneceu uma validação e indicou que este procedimento leva a valores de receptividade mais confiáveis. Dados experimentais da literatura foram tomados para comparação, e as possíveis implicações do gradiente de pressão na evolução da onda TS em um túnel de vento foram avaliadas como uma possível explicação para as diferenças encontradas.

Os resultados apresentados neste trabalho também sugerem que a não linearidade da receptividade dos ressaltos começa a ser significativa em alturas superiores a cerca de 12,6% de δ_b^*. Além disso, a receptividade das cavidades parecia ser menor do que a receptividade do ressalto, o que não foi previsto pelas teorias linearizadas, como a Teoria dos Números Finitos de Reynolds de Choudhari and Streett (1992). Por fim, os resultados mostram que a receptividade diminui com o número de Mach, e esta tendência parece estar de acordo com Raposo, Mughal e Ashowrth (2019).

Palavras-chave: DNS. Receptividade. Acústica. Ressalto. Cavidade. Rugosidade.

ABSTRACT

DOS SANTOS, P. H. R. **Numerical simulation of the receptivity of Tollmien-Schlichting waves due to acoustic waves inciding on rectangular hump and gap in compressible flow**. 2022. 76p. Dissertation (Master) - São Carlos School of Engineering, University of São Paulo, São Carlos, 2022.

The acoustic receptivity of TS waves due to localized roughness (gaps and bumps) inside a compressible laminar boundary layer has been studied. The method utilized was Direct Numerical Simulation with high-order compact finite differences and body fitting mesh. The parameter space covered small rectangular positive or negative non uniformities, and an initial non-linear bump height, as well as different Mach numbers.

A novel way to measure the receptivity was suggested. The comparison with the simulation data from the literature provided a validation and indicated that this procedure leads to more reliable values of receptivity. Experimental data from literature was taken for comparison, and the possible implications of the pressure gradient in the evolution of the TS wave in a wind tunnel were evaluated as a possible explanation for the differences encountered.

The results showed in this paper also suggest that the non linearity of the receptivity of bumps starts to be significant at height greater about 12.6% of δ_b^* (undisturbed Blasius displacement thickness). Moreover, the receptivity of gaps seemed to be smaller than the receptivity of bump, which was not predicted by the linearised theories, such as the Finite Reynolds Number Theory of Choudhari and Streett (1992). At last, the results show that the receptivity decreases with the Mach number, and this trend appears to be in agreement with Raposo, Mughal and Ashworth (2019).

Keywords: DNS. Receptivity. Acoustic. Bump. Cavity. Roughness.

LIST OF FIGURES

LIST OF TABLES

LIST OF ABBREVIATIONS AND ACRONYMS

GATT	Aeroacoustics and Transition to Turbulence Group
LANT	Low Acoustic Noise and Turbulence Wind Tunnel
TS	Tollmien-Schlichting Wave
AC	Acoustic Wave
USP	University of São Paulo
NLF	Natural Laminar Flow
FRNT	Finite Reynolds Number theory
DNS	Direct Numerical Simulation
Re	Reynolds Number
Ma	Mach Number
F	Non-Dimensional Frequency
f_{exc}	Dimensional Frequency

LIST OF SYMBOLS

α *streamwise* wave number

δ_b^* undisturbed Blasius' boundary layer displacement thickness

$Re_{\delta_b^*}$ Reynolds number based on the displacement thickness of the undisturbed Blasius profile

ν Cinematic Viscosity

ω Non-Dimensional Angular Frequency

γ Specific Heat Ratio

CONTENTS

1 INTRODUCTION

1.1 Purpose

A fluid that flows outside a real surface, such as a plane, car or boat, is subject to surface imperfections - roughness, rivets, among others. These imperfections can affect the stability of the laminar flow regime and consequently interfere in the laminar-turbulent transition of the the boundary layer. In the turbulent boundary layer, the fluctuations transport the momentum between the streamlines, which increases the effective shear stress (FOX; PRITCHARD; MCDONALD, 2014), and therefore increases the friction drag on the vehicle, resulting in higher fuel consumption and worse efficiency.

According to Reneaux (2004), it is estimated that the fuel cost represents about 22% of the direct operational cost (DOC) of an air-line, and that a 1% reduction of the drag could lead to a 0.2% reduction in DOC or a 1.6 ton increase in payload, which could result in an increase in the order of 10 passengers for an Airbus A320. Based on this aircraft, the study by Marec (2001) concludes that friction drag corresponds to about 50% of the total, of which 25% comes from the wings. Raposo, Mughal and Ashworth (2019) say that it is possible to achieve a 5% reduction in fuel consumption by extending the region of laminar boundary layer. Although the mechanisms that underpin the turbulence are not fully understood, one may rely on the process which leads to the transition from laminar to turbulent flow to optimize a vehicle design for enhanced energetic efficiency.

It is acknowledged that, in low-disturbance environments, the laminar-turbulent transition has three stages: receptivity, instability growth, and breakdown (SARIC; REED; KERSCHEN, 2002). The term "receptivity" traces back to Morkovin (1969), and it stands for the introduction of wave instabilities into the boundary layer. In low-disturbances environments, such as the atmospheric flight of an airliner, the unstable waves introduced via receptivity amplify mostly through linear modes. However, in higher disturbances scenarios, it is possible to occur bypass transition (MORKOVIN, 1994). Ultimately, these waves amplify, and non-linear effects arise, giving birth to the breakdown of turbulence.

In this scenario, there is interest in the aeronautical industry for studies with the objective of developing means to reduce drag but maintaining a good relation between cost and benefit. In Reneaux (2004) there is a review about the lines of research in this area, and among the alternatives is the possibility of optimizing the geometry of the wing or empennage to extend the region with laminar flow. The aforementioned study states that this passive alternative, when combined with active solutions, such as boundary layer suction, has the greatest potential for reducing drag by 10%. Furthermore, Reed, Saric and Arnal (1996) estimate that if laminar flow could be maintained over the wings of a

large civil transport aircraft, fuel savings of up to 25% could be achieved.

The use of Natural Laminar Flow (*Natural Laminar Flow*, NLF) in a project requires smaller tolerances for errors and deviations in manufacturing, both in surface finishing and in the parts joints. The lack of understanding of the effect of imperfections in the flow means that these tolerances end up being stricter than necessary, generating higher costs in manufacturing and maintenance. A better understanding of how the transition is affected by small cavities or roughness can enable a good balance between the drag reduction by the presence of laminar flow and the cost and weight reductions by lower manufacturing and maintenance costs.

A unit of measurement used for the drag is the *Drag Count* (*DC*), where each unit is equivalent to a 0.0001 change in the drag coefficient (C_D) of the aircraft. In cruise, a typical value is between 200 and 400 *DC*. A desired precision for the drag estimates is 10 *DC* for subsonic regimes, 4 *DC* for transonic and 1 *DC* for supersonic regimes. Methods currently used by the industry have an error in the drag estimate of the order of 10%, or even more in transonic cases (KAYNAK; EMRE, 2008). These values shows a contrast between the current ability to correctly predict the drag and the precision necessary for an effective reduction of fuel consumption and operational costs.

According to Reed, Saric and Arnal (1996), understanding the transition is necessary for the exact prediction of aerodynamic forces and of heating. In the case of an aeronautical design, a good prediction of the transition point is of great importance, as it influences the total drag of the aircraft, which impacts its fuel consumption.

There are semi-empirical methods based on linear growth (Ingen (1956) and Smith (1956)) which are utilized to predict this transition point, however these methods bypass the receptivity stage by requiring a calibration of the critical N-factor (RAPOSO; MUGHAL; ASHWORTH, 2018). which may not be available in early stages of a vehicle design. The development of a receptivity prediction tool is, therefore, necessary for a robust transition prediction.

1.2   Objectives

While there is a recent research effort on compressibility effects in the receptivity and on its non-linear behaviour, there is little numerical data regarding rectangular roughness elements and gaps depth. In this context, the general objective of this paper is to perform numerical simulations of the acoustic waves passing over localized roughness within boundary layers in order to assess the non-linear receptivity regime.

1.3 Work structure

The remainder of this work is structured as follows. Chapter 2 presents a literature review on the topic. Chapter 3 describes the methodology utilized, including the parameter space. Chapter 4 discusses the numerical uncertainty associated with the Direct Numerical Simulation (DNS) results presented. Chapter 5 provides a preliminary discussion about the physical phenomena and presents comparison with literature. Chapter 6 shows the result for different humps and gaps depths, and for different Mach numbers. At last, Chapter 7 draws some conclusions from the work.

2 LITERATURE REVIEW

The transition from a laminar flow to a turbulent flow has been the subject of study for many decades, but it still remains an open problem. The first studies on the laminar-turbulent transition began around the end of the 19th century, with names such as Rayleigh (1879), Reynolds (1883) and Prandtl (1904).

The presence of small perturbations in a two-dimensional boundary layer in the laminar flow regime causes the formation of instability waves known as Tollmien-Schlichting waves (*Tollmien-Schlichting waves*, TS), which appear in the flow in the first stage of natural transition (Fig. 1).
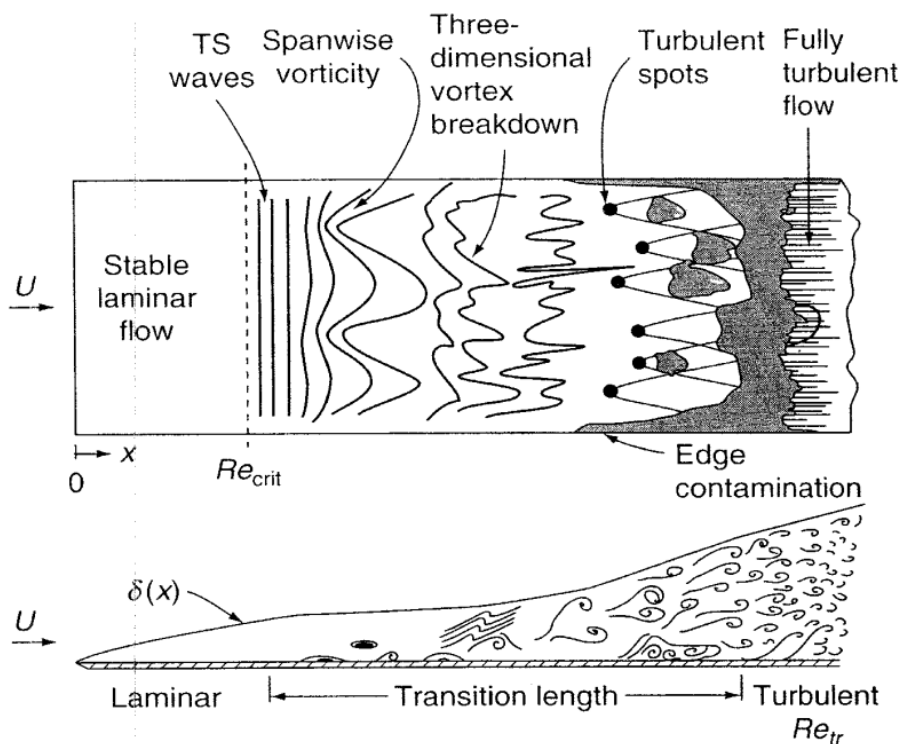
Figure 1 – The stages of a natural transition from the laminar to the turbulent regime.
Source: White and Corfield (2006)

The study of the laminar-turbulent transition in the boundary layer is divided into two categories. The first category of study focuses on the propagation of these waves and on the analysis of the stability of the flow. In the case of a spatially-unstable flow, these waves are amplified as they are convected downstream. When these oscillations are small, up to 0.1% of the magnitude of free flow, the nonlinear effects are small and the theory of linear stability (*Linear Stability Theory*, LST) can well predict the flow behaviour.

The second category focuses on receptivity, which is the process by which external

disturbances (acoustic waves, vorticity, vibration, among others) enter in the boundary layer and transfer part of their energy to instability waves, which may have different characteristic length and speed. Depending on the magnitude of the disturbance, the transition in a boundary layer occurs in one of the ways indicated in Figure 2.
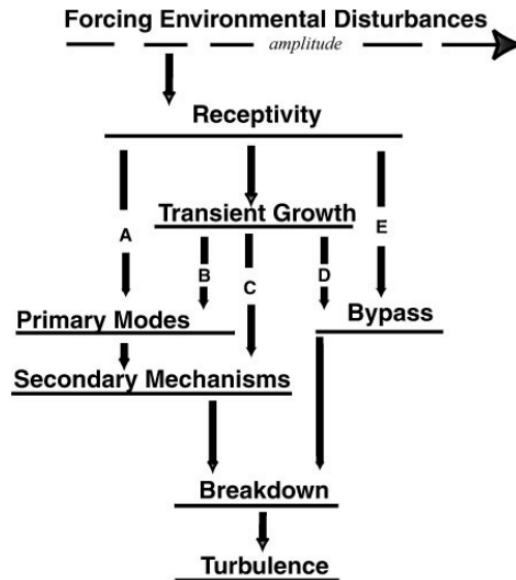
Figure 2 – Typical routes of receptivity to turbulence in a boundary layer.
Source: Saric, Reed and Kerschen (2002)

The theoretical works of Ruban (1984), Goldstein (1983) and Goldstein (1985) were one of the first to address the receptivity calculation. They demonstrated, using asymptotic expansions and triple-deck formalism, that the receptivity is prone to occur in regions of rapid change in mean flow, such as in the leading edge or the near field of surface non uniformities. There is a scale conversion mechanism in these regions, as the external disturbances usually have a different wavelength from the instabilities modes. Thus, this mechanism determines the initial amplitude, phase, and frequency of the instability waves. Furthermore, it was stated by these studies that the leading edge receptivity is significantly weaker when compared with surface roughness receptivity.

In the following decade, Choudhari (1993), Choudhari and Streett (1992) and Crouch (1992) developed the so-called Finite Reynolds Number theory (FRNT), and it has allowed the receptivity calculation to account for different Reynolds number and frequencies in comparison with the asymptotic theory. However, the FRNT utilizes an incompressible set of governing equations and does not account for the effects of the non-parallelism in the undisturbed mean flow.

Years later, Raposo, Mughal and Ashworth (2018) and Raposo, Mughal and Ashworth (2019) developed an Adjoint Harmonic Linearised Navier-Stokes approach based on the FRNT. This approach showed remarkable performance and excellent agreement with

the previous studies, whilst extending the analysis to both the effects of the compressibility and non-parallelism in the mean flow. They reported a strong dependence on Mach number, roughness streamwise position and acoustic non-dimensional frequency, $F = (2\pi f_{exc}\nu)/U_\infty^2$, on the receptivity. In this equation, f_{exc} is the dimensional frequency in Hertz, ν is the kinematic viscosity and U_∞ is the free stream velocity. The difference of the receptivity between a localized roughness at the first branch in a flow with Mach number 0.1 and 0.5, both with $F = 20 \times 10^{-6}$, changed by a factor of 2.2, approximately. The reader is referred to Raposo, Mughal and Ashworth (2018) to a more comprehensive review on the topic of adjoint solutions.

The receptivity of acoustic waves on boundary layers has also been subject to a number of experimental works (e.g., Saric (1994), Saric and White (1998), Monschke, Kuester and White (2016), Placidi, Gaster and Atkin (2020)). They utilized a variety of approaches to measure the instability wave due to acoustic receptivity, and each of these approaches has limitations either on the robustness, accuracy, or acquisition procedure.

Saric (1994) presents a study on the receptivity of acoustic waves to thin mylar strips on the flat plate. The strip was placed at X = 460 mm where $\sqrt{Re_x} = 590$. The acoustic frequency was kept constant at $F \approx 50 \times 10^{-6}$, while the thickness of the roughness element varied from 45 to 270 μm and the acoustic wave amplitude varied between 90dB and 100dB. It was reported a departure from linear behavior with respect to the element height at about $h = 200\mu m$, which corresponds to $h/\delta_b^* \approx 0.15$. It was also reported a non-linear dependence of the TS amplitude with the acoustic amplitude. However, Nayfeh and Ashour (1994) developed a numerical method based on the Interacting Boundary Layer (IBL) equations, and they pointed out that this non-linearity observed by Saric (1994) may be due to interference of TS waves generated at the leading edge. Notwithstanding, both papers attribute the non linear height dependence to the presence of recirculating bubbles after the roughness.

Years later, Monschke, Kuester and White (2016) developed a biorthogonal decomposition method for the TS extraction based on the projection of the measured flow field into the solution of a modified Orr-Sommerfeld equation which also accounts for the Stokes Wave. They utilized an active noise cancelling apparatus aiming the upstream travelling acoustic waves for improved measurement accuracy. While the results for leading edge receptivity do not seem to be precise, they showed a good agreement for the receptivity of a hump. This method is can be also utilized in numerical works.

More recently, Placidi, Gaster and Atkin (2020) built a procedure based on a two-dimensional roughness with adjustable height to bypass some of the limitations of the previous works. This procedure allowed the measurement of acoustic receptivity of gaps, which had not been addressed in other studies before. Their results showed good agreement for small roughness heights with the data from the code described by Raposo,

Mughal and Ashworth (2019). As expected, their results presented a departure from the predicted receptivity of their beaspoke linearised simulation at about $h > 0.126\delta_b^*$. Placidi, Gaster and Atkin (2020) also attributed this discrepancy to the presence of a recirculation bubble. Following the conclusions of Bodonyi (1990) and Nayfeh and Ashour (1994), this recirculating bubble might not have been present in the reference simulation utilized by Placidi, Gaster and Atkin (2020).

On the other hand, numerical studies provided some relevant results with a recent progress in compressible subsonic regime (see Würz *et al.* (2003a), Kurz and Kloker (2014), DE TULLIO and Ruban (2015)). Würz *et al.* (2003a) conducted a DNS of acoustic receptivity of a 3D roughness in a 2D boundary layer. To validate their code, at first the 2D roughness case was compared with the Choudhary's FRNT, and remarkable agreement was observed. Their 2D roughness case is compared with the results in this present work.

DE TULLIO and Ruban (2015) presents a DNS of the receptivity of acoustic waves on a localized bump with a gaussian shape. The base flow was obtained with the full Navier Stokes equations, however the unsteady wave was simulated in a linearised set of equations. They compared the results from the asymptotic theory and they found good agreement. They also extended the analysis to different roughness height and found that at about $h/\delta_b^* = 0.17$ the receptivity nonlinearity becomes significant, which is somewhat in agreement with Saric (1994) and Placidi, Gaster and Atkin (2020). They also pointed out that this upper bound height might be independent of the Reynolds number. It may be worth noting that Kurz and Kloker (2014), who studied the effect of the steady wave disturbance by DNS means, identified that the nonlinearity might be present even at the smallest roughness height.

In what concerns the effect of the gap in acoustic receptivity, there are few DNS references in literature. Nonetheless, the study of the steady wave disturbance caused by humps and gaps conducted by Choudhari and Duck (1996) suggests that the effect of non linear height of gaps is different from the humps, being the former significantly lower than the latter.

3 METHODOLOGY

3.1 Computational domain and parametric space

The present work performed DNS with a high-order finite difference scheme. The geometries were flat plates with and without roughness. The computational model is shown in Fig. 3.

Outerflow
$$\frac{\partial[u,v,w,T,P]}{\partial y} = 0$$

Acoustic wave

Buffer zone

Boundary layer edge

Tollmien-Schilichting wave

Inflow
$u = 1 + u'_{ac};$
$v, w = 0;$
$T = T_\infty + T'_{ac};$
$\frac{\partial P}{\partial x} = 0;$

Free slip and no penetration
$\frac{\partial[u,P]}{\partial y} = 0;$
$v, w = 0;$
$T = T_\infty$

No slip and no penetration wall
$u, v, w = 0$
$\frac{\partial P}{\partial n} = 0$

Outflow
$\frac{\partial^2[u,v,w,T]}{\partial x^2} = 0;$
$P = P_\infty$
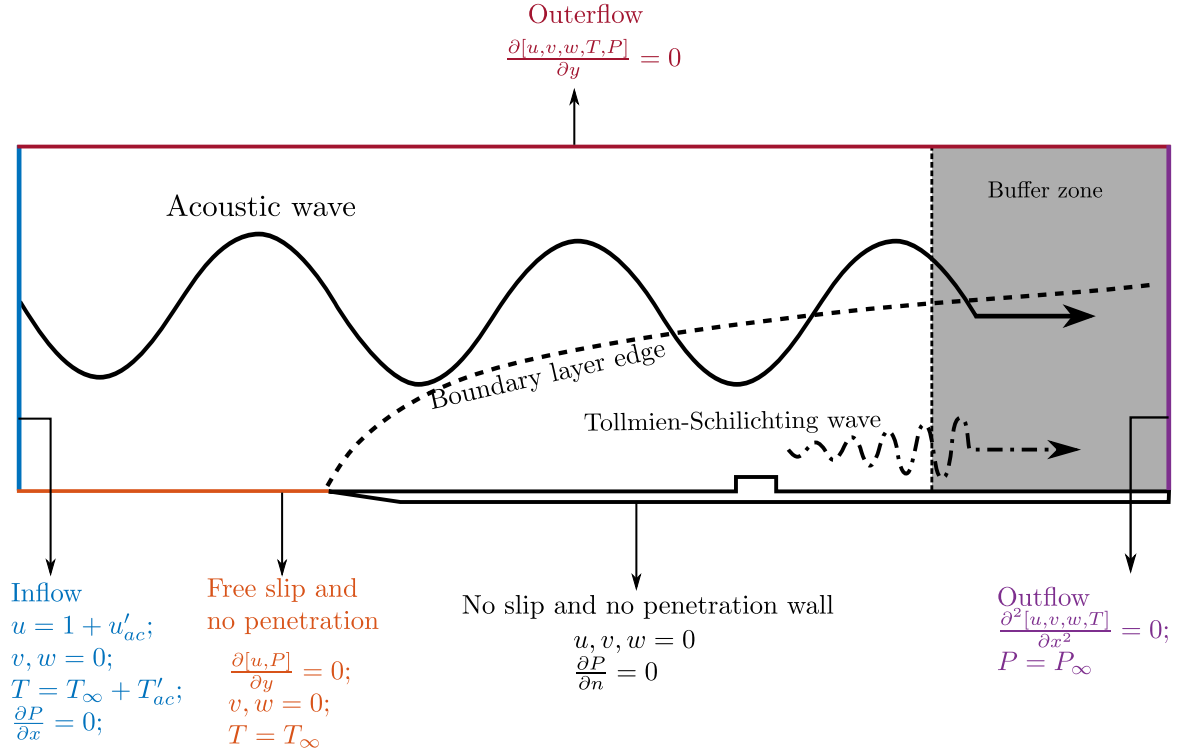
Figure 3 – Geometry and boundary conditions of the computational model

The relevant flow parameters are summarized in Tab. 1, 2 and 3. It reports the following non-dimensional numbers: $Re_{\delta_b^*} = U_\infty \delta_b^*/\nu$, Ma, $F = 2\pi * f_{exc}\nu/U_\infty^2 = \omega/Re_{\delta_b^*}$. These numbers are the Reynolds number based on the displacement thickness of the undisturbed Blasius' profile, δ_b^*, the Mach number, and the non-dimensional frequency. h and w are the roughness's height and width, respectively. These parameters are calculated at the position of the upstream edge of the roughness. The useful domain range is [-100 1200]x[0 38], in terms of δ_b^*.

The base flows obtained were superimposed by a sinusoidal wave at the inflow boundary condition. It has a constant non-dimensional frequency and an amplitude at most of $O(U_\infty \times 10^{-3})$, where U is the reference far-field velocity. This amplitude was verified to be inside the linear regime of the receptivity (i.e., the receptivity coefficient varied linearly with the acoustic wave amplitude, as depicted in Sec. 5.1). The TS generated via

Table 1 – flow parameters for bump height study

Name	$Re_{\delta_b^*}$	Ma	$F \times 10^6$	h/δ_b^*	w/δ_b^*
b04m1	1413.8	0.1	25.85	4.20%	16.80
b08m1	1413.8	0.1	25.85	8.28%	16.80
b12m1	1413.8	0.1	25.85	12.6%	16.80
b33m1	1413.8	0.1	25.85	33.3%	16.80

Table 2 – flow parameters for gap depth study

Name	$Re_{\delta_b^*}$	Ma	$F \times 10^6$	h/δ_b^*	w/δ_b^*
c04m1	1413.8	0.1	25.85	-4.20%	16.80
c08m1	1413.8	0.1	25.85	-8.28%	16.80
c12m1	1413.8	0.1	25.85	-12.6%	16.80

Table 3 – flow parameters for mach study

Name	$Re_{\delta_b^*}$	Ma	$F \times 10^6$	h/δ_b^*	w/δ_b^*
b12m1	1413.8	0.1	25.85	12.6%	16.80
b12m2	1413.8	0.2	25.85	12.6%	16.80
b12m6	1413.8	0.6	25.85	12.6%	16.80
b12m8	1413.8	0.8	25.85	12.6%	16.80

receptivity were filtered out using the subtraction between the fluctuations from the cases with and without roughness.

3.2 Governing Equations

The Eqs. 3.1 to 3.3 present the Navier-Stokes equations, which are solved numerically. In these equations, ρ is the specific mass, t is time, u_i is the velocity in the x_i direction, p is the pressure, τ_{ij} is shear stress, e is the internal energy, and q_i is the heat flow in the x_i direction.

$$\frac{\partial \rho}{\partial t} = -\rho \frac{\partial u_i}{\partial x_i} - \frac{\partial \rho}{\partial x_i} u_i \tag{3.1}$$

$$\frac{\partial u_j}{\partial t} = -\frac{\partial u_j}{\partial x_i} u_i - \frac{1}{\rho} \frac{\partial p}{\partial x_j} + \frac{1}{\rho} \frac{\partial \tau_{ij}}{\partial x_i} \tag{3.2}$$

$$\frac{\partial e}{\partial t} = -\frac{\partial e}{\partial x_i} u_i - \frac{p}{\rho} \frac{\partial u_i}{\partial x_i} + \frac{1}{\rho} \tau_{ij} \frac{\partial u_j}{x_i} - \frac{1}{\rho} \frac{\partial q_i}{\partial x_i} \tag{3.3}$$

Constitutive equations are used to close the system of equations. The hypotheses are that the flow is a perfect gas, which leads to Eq. 3.4 and 3.5. In these equations, T is temperature, Ma_∞ is the Mach number, γ is the specific heat ratio.

$$T = e\gamma (\gamma - 1) \mathrm{Ma}_\infty^2 \tag{3.4}$$

$$p = (\gamma - 1)\, \rho e \tag{3.5}$$

Sutherland's law (Eq. 3.6) is utilized to calculate the viscosity. In this equation, μ is the dynamic viscosity, $C = \frac{110K}{T_\infty^*}$ and $T_\infty^* = 300K$.

$$\frac{\mu^*}{\mu_\infty} = \mu(T) = \frac{1+C}{T+C} T^{\frac{3}{2}} \tag{3.6}$$

The viscous tension tensor and the heat flux are calculated from Eq. 3.7 and 3.8. Re is the Reynolds number in these equations, and Pr is the Prandtl number.

$$\tau_{ij} = \frac{\mu(T)}{\mathrm{Re}} \left(\frac{\partial u_i}{\partial x_j} + \frac{\partial u_j}{\partial x_i} - \frac{2}{3}\delta_{ij} \frac{\partial u_k}{\partial x_k} \right) \tag{3.7}$$

$$q_i = -\frac{\mu}{(\gamma - 1)\,\mathrm{Re}\,\mathrm{Pr}\,\mathrm{Ma}_\infty} \tag{3.8}$$

3.3 Boundary conditions including acoustics

The boundary conditions are described in Fig. 3. The flat plate and the roughness walls have no-slip and no-penetration boundary conditions, zero pressure gradient in the normal direction, and constant temperature. The pressure in both roughness' corners nodes is set to the average pressure that meets the boundary condition for each direction. Upstream of the flat plate, there is a free-slip region to accommodate the free flow before the leading edge of the no-slip wall.

The top boundary has a null Neumann boundary condition. The second derivatives, except for the pressure itself, are set to zero in the outflow. The pressure is defined with the Dirichlet boundary condition in the outflow and null Neumann in the inflow.

For the acoustic wave, a harmonic perturbation is superimposed at the inflow. The wave is inserted in the velocity, density, and energy variables matching the free-stream acoustic impedance for a sinusoidal wave. A buffer zone downstream exists, so oscillations are neither reflected nor amplified.

Figure 4 presents the free stream disturbed by a 3-wavelength acoustic wave multiplied by a Gaussian function. The dashed line is the buffer zone's limit, and the contour plot is in absolute value and logarithmic scale. The bufferzone length was adjusted to damper the acoustic wave by a factor of at least 1/1000, so not to introduce reflections.

In Figure 5, the simulated acoustic wave's amplitude and phase are plotted. It is possible to see that the acoustic wave has negligible amplitude decay over the useful domain of the flat plate, and the phase varies linearly.
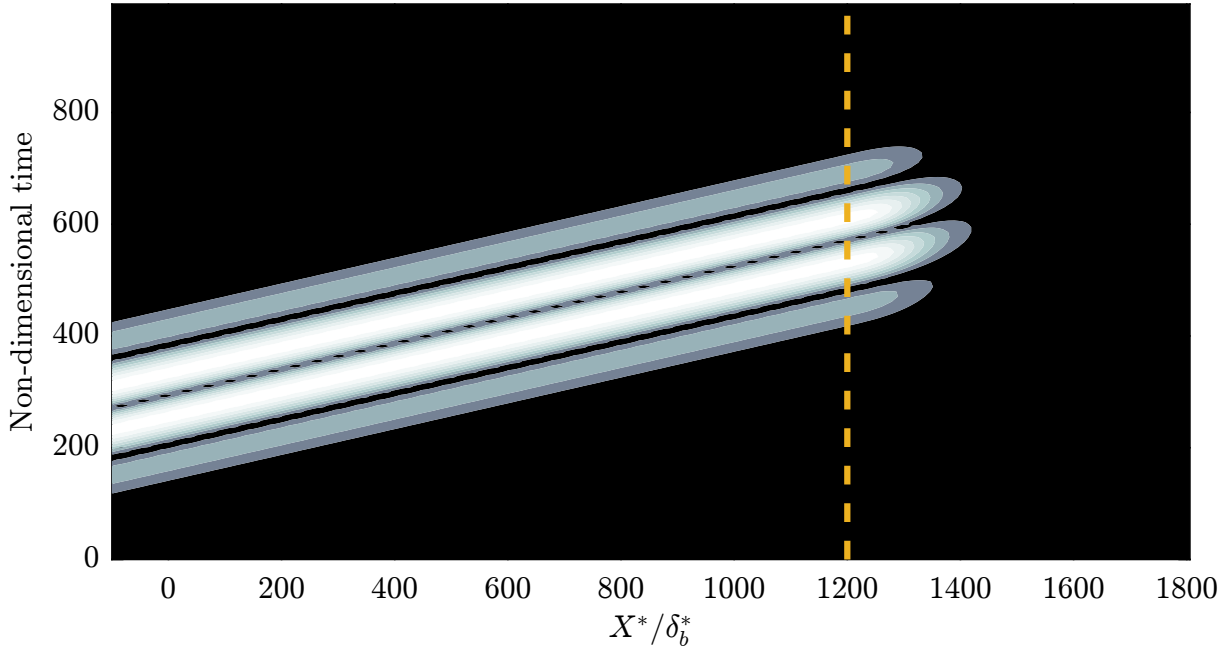
Figure 4 – Contour plot of the disturbance generated by a 3-wavelength acoustic wave multiplied by a Gaussian in the free-stream. The dashed line is the buffer zone's limit. The contour plot is in absolute value and logarithmic scale.
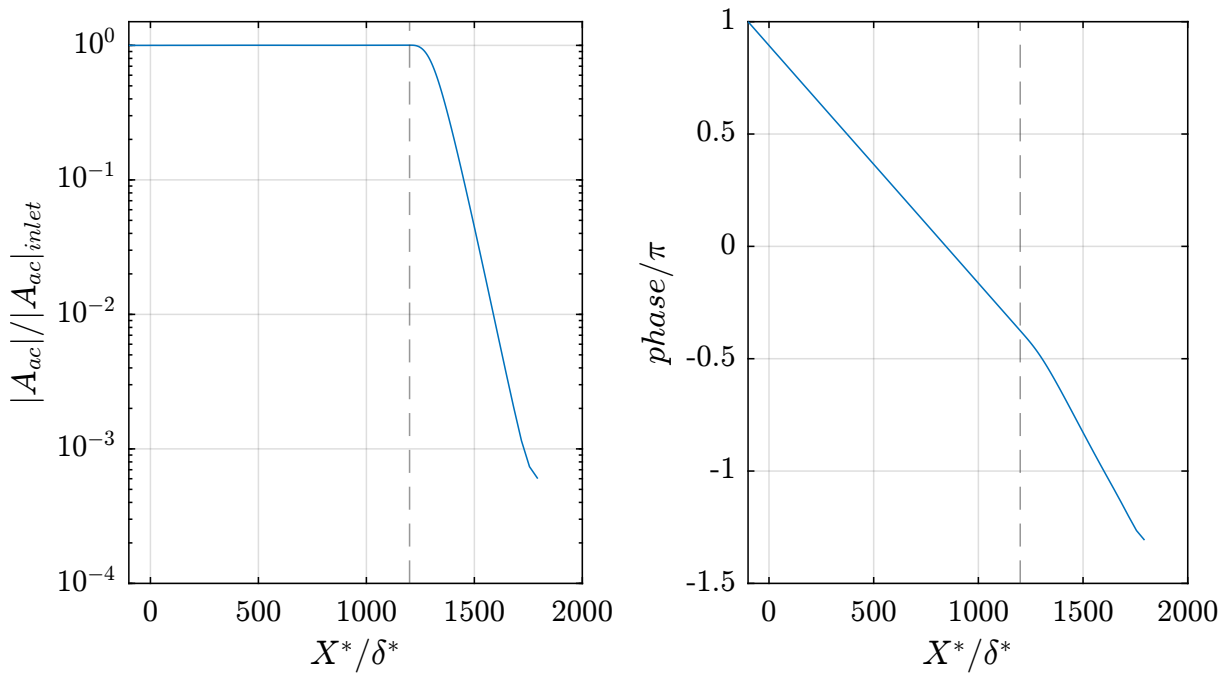
Figure 5 – amplitude (left) and phase (right) of the simulated acoustic wave in the free stream. The dashed line indicates the buffer zone.

3.4 Numerical Scheme

The Aeroacoustics, Transition and Turbulence Research Group (GATT) currently has three high-performance computers where the computational analyzes are performed. The code used for the flow simulation solves the compressible Navier-Stokes equations

numeracly without the use of turbulence model. Therefore, it is known as *Direct Numerical Simulation*. It was developed by this research group (BERGAMO, 2014; MARTINEZ; MEDEIROS, 2016; MATHIAS; MEDEIROS, 2018). In DNS, the primitive variables of Eq. 3.1 to 3.3 are calculated at each domain point in dimensionless form. The simulation routines are written in FORTRAN 90. Their main features are listed below:

- Spectral and high-order spatial derivatives (LELE, 1992)
- Time integration by the Runge-Kutta method up to the fourth order
- Cartesian mesh with refinement in regions of interest
- Spatial low-pass filter to avoid *aliasing* problems (GAITONDE; VISBAL, 1998)
- Low-pass temporal filter to accelerate convergence to a steady state, if necessary (ÅKERVIK *et al.*, 2006)
- Buffer zones on open contours to avoid unwanted reflections
- Parallel execution using domain splitting techniques using MPI (LI; LAIZET, 2010)
- Parallelized execution by multiprocessçprogram using OpenMP

The subsequent sections explain in detail the numerical methodology used. For more details of the DNS scheme, the reader is refereed to Martinez and Medeiros (2016) and Mathias and Medeiros (2018)

3.4.1   Spatial derivatives

Finite differences calculate the spatial derivatives according to the sixth-order spectral scheme described by Lele (1992). An advantage of the spectral scheme is the better approximation of the flow derivative for a broader spectrum of frequencies.

Despite achieving high order of formal approximation, explicit schemes quickly lose precision at high wave numbers due to the higher-order derivatives.

This scheme uses Eq. 3.9. In this equation, α, β, a, b, and c are adjustable parameters according to the order of approximation of the derivative. h is the mesh spacing, u_i is the value of the property at the point X_i and u_i' is its approximate first derivative. Near the borders, the stencil is adjusted and becomes decentralized.

$$\beta u'_{i-2} + \alpha u'_{i-1} + u' + \alpha u'_{i+1} + \beta u'_{i+1} = a\frac{u_{i+1} - u_{i-1}}{2h} + b\frac{u_{i+2} - u_{i-2}}{4h} + \frac{u_{i+3} - u_{i-3}}{6h} \quad (3.9)$$

The order of approximation of this scheme is given by Eq. 3.10 (LELE, 1992).

$$\begin{aligned}
\text{Second order:} \quad & a + b + c & = & \quad 1 + 2(\alpha + \beta) \\
\text{Fourth order:} \quad & a + 2^2 b + 3^2 c & = & \quad 6(\alpha + 2^2 \beta) \\
\text{Sixth order:} \quad & a + 2^4 b + 3^4 c & = & \quad 10(\alpha + 2^4 \beta) \\
\text{Eigth order:} \quad & a + 2^6 b + 3^6 c & = & \quad 14(\alpha + 2^6 \beta)
\end{aligned} \tag{3.10}$$

The system becomes explicit if α and β are null. In this case, if $a = 1$, $b = 0$, and $c = 0$, the derivative scheme becomes second-order explicit. For example, an explicit fourth-order scheme has $a = 4/3$ and $b = -1/3$.

In the bufferzone, the derivative scheme is replaced by the explicit second-order one. This transition is gradual and cosine, with the first point of the bufferzone being calculated with the high-order method and the last point with the low-order method.

Eq. 3.9 is used when the mesh spacing is uniform. However, the mesh used in the simulations has refinement. To solve this problem, we used the chain rule to map the position X_i of the refined mesh's points in a domain with a mesh with uniform spacing, ϕ_i (Eq. 3.11).

$$\frac{\partial u}{\partial x} = \frac{\partial u}{\partial \phi} \frac{\partial \phi}{\partial x} \tag{3.11}$$

In Eq. 3.11, u is the value of the function, x is the position of the real mesh, ϕ is an equally spaced intermediate mesh, with $h = 1$. Therefore, both terms in Eq. 3.11 can be obtained by finite differences. Furthermore, the right side only needs to be calculated once as the mesh is not changed during the simulation.

3.4.2 Time marching

A fourth-order Runge-Kutta scheme performs the temporal integration with a fixed time step dt. This scheme is given by Eq. 3.12. In this equation, $\mathbf{U}^n$ is the flow in the time step n.

$$\mathbf{U}^{n+1} = \mathbf{U}^n + \frac{\Delta t}{6} \left(\mathbf{K}_1 + 2\mathbf{K}_2 + 2\mathbf{K}_3 + \mathbf{K}_4 \right) \tag{3.12}$$

$$\mathbf{K}_1 = \mathbf{f}(\mathbf{U}^n) \tag{3.13}$$

$$\mathbf{K}_2 = \mathbf{f}\left(\mathbf{U}^n + \frac{\Delta t}{2} \mathbf{K}_1 \right) \tag{3.14}$$

$$\mathbf{K}_3 = \mathbf{f}\left(\mathbf{U}^n + \frac{\Delta t}{2} \mathbf{K}_2 \right) \tag{3.15}$$

$$\mathbf{K}_4 = \mathbf{f}(\mathbf{U}^n + \Delta t \mathbf{K}_3) \tag{3.16}$$

The boundary conditions are reinforced at each sub-time step, totalling four applications for each time step. The numerical stability of the code limits the largest possible Δt time step. The Courant-Friedrichs-Lewy (CFL) condition is defined in Eq. 3.17. For the fourth-order Runge-Kutta scheme, a CFL of approximately 1.3 keeps the simulation stable.

$$\Delta t \leq \frac{CFL_{max}}{\left(\frac{1/Ma+u_{max}}{\Delta x_{min}} + \frac{1/Ma+v_{max}}{\Delta y_{min}} + \frac{1/Ma+w_{max}}{\Delta z_{min}}\right)} \tag{3.17}$$

Eq. 3.17 shows that for small Ma numbers the time step Δt needs to be small. At numbers of Ma close to the incompressible flow, the Δt must be significantly reduced. Thus, it is computationally more expensive to simulate a case with small Ma with the compressible formulation of the Navier-Stokes equations.

For the flow's diffusive characteristics, the simulation's stability can be obtained respecting Eq. 3.18.

$$\Delta t \leq \frac{Re}{\left(\frac{1}{\Delta x_{min}^2} + \frac{1}{\Delta y_{min}^2} + \frac{1}{\Delta z_{min}^2}\right)} \tag{3.18}$$

3.4.3 Spatial filter *anti-aliasing*

In real flows, there are physical mechanisms of energy transfer from larger scales to smaller scales until reaching the level of molecular energy dissipation, which generates heat. However, it is not always possible to have a sufficiently refined mesh to capture these small scale effects, generating aliasing issues. Eriksson and Rizzi (1985) state that, due to the effect of *aliasing*, the movement of smaller scales solved by the simulation is transferred numerically to larger scales. This transference can cause a divergence between the actual flow and the numerical result. As a result, high-frequency noise can appear in the simulation, and it can accumulate and cause numerical instability and divergence in the simulation.

It is known that a mesh can resolve waves with a wavelength at least twice the spacing of the points. Waves with shorter wavelengths can cause *aliasing*. However, filtering should be enough to dissipate high-wave number noise, so a numerical low-pass filter is implemented in the code. This filter is based on the work of Gaitonde and Visbal (1998). Its strength can be adjusted in the pre-processing phase and, ideally, should be as weak as possible, to minimize its effects on the result. This filter is disabled close to the boundaries and the wall because the derivatives are more prominent in these regions. Large derivatives hurt the *antialiasing* filtering process.

The implementation of the low-pass filter *antialiasing* is similar to the implementation of the derivative calculation. Eq. 3.19 generates the linear system to be solved at the end of each time step. In this equation, $\bar{u}$ is the function after filtering, u_i is the value of the function before the filter at the point X_i, α_f and the parameter referring the strength of the filter, which can vary between -0.5 (equivalent to no filter) and 0.5 (maximum strength).

$$\alpha_f \bar{u}_{i-1} + \bar{u}_i + \alpha_f \bar{u}_{i+1} = \sum_{n=0}^{N} \frac{a_n}{2} \left(u_{i-n} + u_{i+n} \right) \tag{3.19}$$

For the scheme used, the values of the coefficients a_n are presented in Eq. 3.20.

$$
\begin{aligned}
a_0 &= \frac{193 + 126\alpha_f}{256} \\
a_1 &= \frac{105 + 320\alpha_f}{256} \\
a_2 &= \frac{-15 + 30\alpha_f}{64} \\
a_3 &= \frac{45 - 2\alpha_f}{512} \\
a_4 &= \frac{-5 + 10\alpha_f}{256} \\
a_5 &= \frac{1 - 2\alpha_f}{512}
\end{aligned}
\tag{3.20}
$$

3.5 Parallel computation

The DNS code used in this work was developed *in-house* by the GATT over several years. The pre-processing and post-processing are done in Matlab and include the following steps:

- Receive the input parameters
- Create a directory for the results and initialize log files
- Generate the mesh
- Identify walls immersed in the domain
- Set up the boundary conditions
- Set up matrices with coefficients for the spatial derivatives and filters
- Create the initial flow

The processing is done in FORTRAN, and the compiler used is *gfortran.*

3.5.1 Linear system solver

As explained in previous sections, the computation of the spatial derivatives and the anti-aliasing filter is implicit. It involves solving linear systems with a coefficient matrix in tridiagonal form. The solution to this system is obtained using the Thomas algorithm.

An example of a system with a tridiagonal matrix is presented in Equation 3.21, where y_i are known values, and the solver needs to calculate d_i.

$$
\begin{bmatrix}
b_1 & c_1 & & \cdots & & a_1 \\
a_2 & b_2 & c_2 & & & \vdots \\
& a_3 & b_3 & \ddots & & \\
\vdots & & \ddots & \ddots & c_{n-1} \\
c_n & \cdots & & a_n & b_n
\end{bmatrix}
\begin{bmatrix}
d_1 \\ d_2 \\ \vdots \\ d_n
\end{bmatrix}
=
\begin{bmatrix}
y_1 \\ y_2 \\ \vdots \\ y_n
\end{bmatrix}
\tag{3.21}
$$

When $a_1 = c_n = 0$, the system is not cyclic and, therefore, can be solved by Thomas' algorithm:

```
for i = 2 ... n do
a_i = ai/b_{i - 1}
b_i = bi - a_ic_{i - 1}
y_i = y_i - a_iy_{i - 1}
end for
dn = xn/bn
for i = n - 1 ... 1 do
d_i = (y_i - c_i d_i)/b_i
end for
```

If the system is cyclical, the algorithm proposed by Temperton (1975) is used. The first row of the inverted tridiagonal matrix is computed during pre-processing and it is stored. This row is used to get the value of d_1 from the vector y. The system is then modified for Eq. 3.22, which the Thomas algorithm can solve.

$$
\begin{bmatrix}
b_1 & c_1 & & \cdots & & 0 \\
a_2 & b_2 & c_2 & & & \vdots \\
& a_3 & b_3 & \ddots & & \\
\vdots & & \ddots & \ddots & c_{n-1} \\
0 & \cdots & & a_n & b_n
\end{bmatrix}
\begin{bmatrix}
d_1 \\ d_2 \\ \vdots \\ d_n
\end{bmatrix}
=
\begin{bmatrix}
y_1 - a_1 d_1 \\ y_2 \\ \vdots \\ y_n - c_n d_1
\end{bmatrix}
\tag{3.22}
$$

3.5.2 Parallelization

The code is executed with serial and parallel processing. In the parallelized portion of the code, the 2DECOMPT & FFT library is used, which was written using the MPI protocol. This library is highly scalable and optimized for the best performance (LI; LAIZET, 2010).

The computational domain is divided into slices, as shown in Fig. 6a. This division is also known as *pencil* or *drawer decomposition*. Each slice is allocated to a different process. Local operations are performed in one direction only, and communication is done only within each sub-group.

In order to calculate derivatives in other directions, the domain needs to be transposed in each direction (Fig. 6b and c). The process is illustrated in Fig. 7. The process is illustrated for a three-dimensional simulation in both Fig. 6 and 7. However, this process is adapted for the present two-dimensional situation.
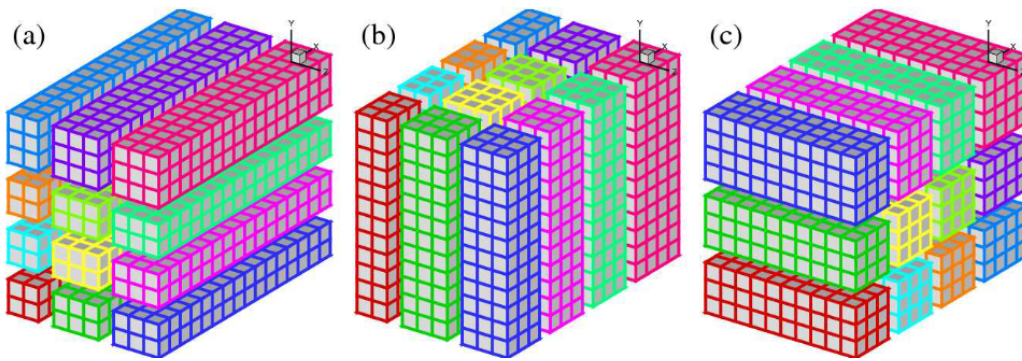

Figure 6 – Illustration of a domain divided into 3x4 processes. Source: Li and Laizet (2010)
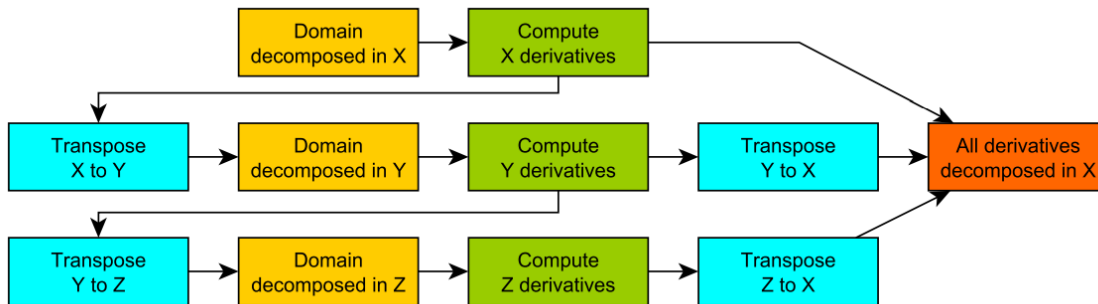
Figure 7 – Calculation of directional derivatives in the domain divided according to *drawer decomposition* method

4 NUMERICAL PRECISION

This chapter evaluates the numerical uncertainty associated with the DNS utilized and the physical phenomenon of interest. In order to accomplish this objective, the *b12m1* case is taken as reference (see Tab. 1), as this case is thought to be representative.

4.1 Mesh refinement description

The code uses structured mesh in a rectangular domain with stretching in both X and Y directions. It is possible to control the strength and size of the stretching, and the grid is much finer close to the wall and roughness. In addition, there are smooth adjustments in the node position to match the roughness' edges. The mesh is shown in Fig. 8.

In order to prepare the computational mesh, best practice for the simulation of TS waves over smooth plates were observed to generate the first mesh. Upon this base mesh, the region near the roughness element was refined, and the numerical precision related to acoustic receptivity is treated in the following sections.

4.2 Grid requirement for the Stokes Layer

The Stokes Layer profile is analyzed in Fig. 9 for different mesh refinements and positions of the plate. There is no discernible difference in the Stokes Layer profile in this figure in both upstream and downstream positions.

4.3 Grid requirement for the roughness

The mesh independence for the receptivity process is presented in Fig. 10. In this figure, the mesh is alternatively refined in the X and Y direction. The upper chart presents the evolution of the TS wave and the bottom chart presents the ratio between the evolutions with different mesh sizes. The difference below 4%, which is considered good enough for the physical phenomena of interest.

However, in obtaining the initial disturbance at the center of the roughness, it is necessary to use the information on the evolution of the TS wave over the rough plate. This evolution needs to be also independent of the mesh. So, Fig. 11 presents the evolution of the TS wave produced by suction and blowing at the wall with different mesh refinements. It is possible to see that the variation is up to 3%, which is also thought to be good enough for the physical phenomena of interest.
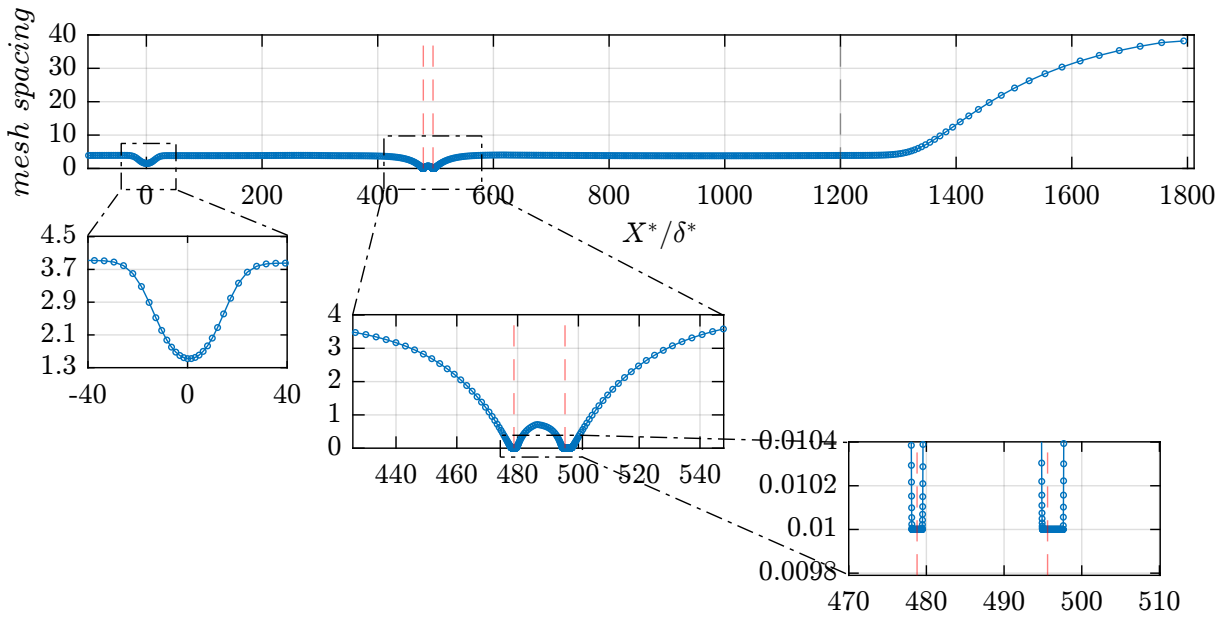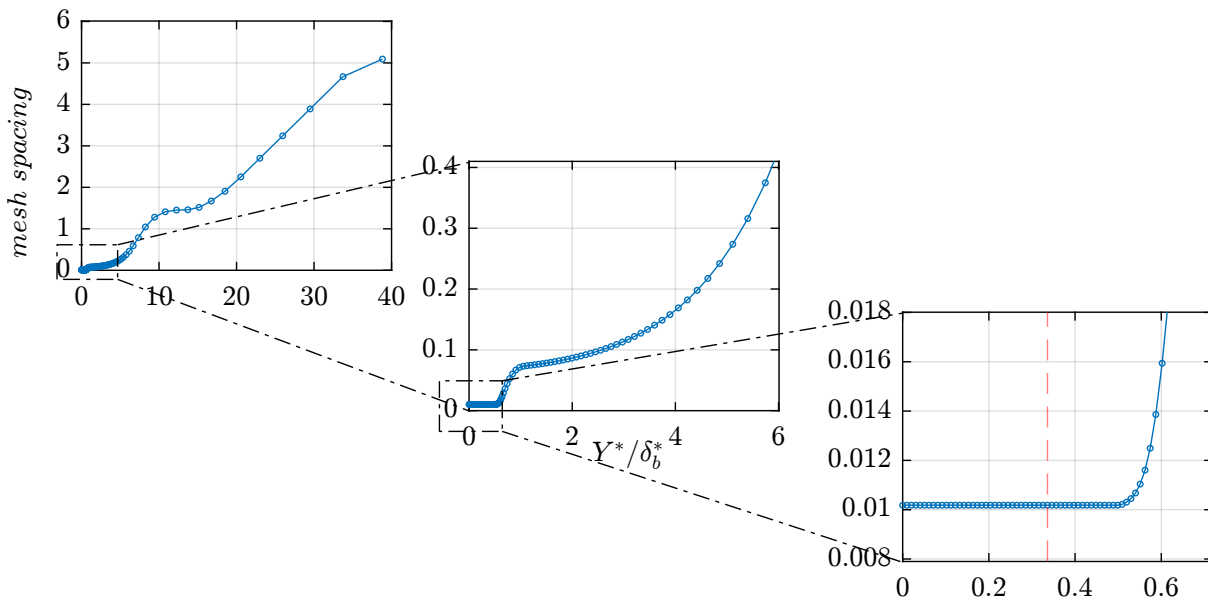
Figure 8 – Mesh utilized in the simulation. a) Mesh in the streamwise direction. b) mesh in the perpendicular direction. There is stretching in both directions.

4.4 Effectively incompressible Mach number

The DNS code utilized was implemented with compressible governing equations, which enables the study of the sensibility of the receptivity to the Mach number. However, when comparing experimental studies, it turned out to be too expensive to simulate the same experimental Mach number because the stability of the code requires tiny time steps. Therefore, in order to accelerate the simulation, the Mach number was increased.

In order to assess the highest Mach number such that the compressibility effects could be neglected, Figure 12 presents the comparison between the evolution of the TS
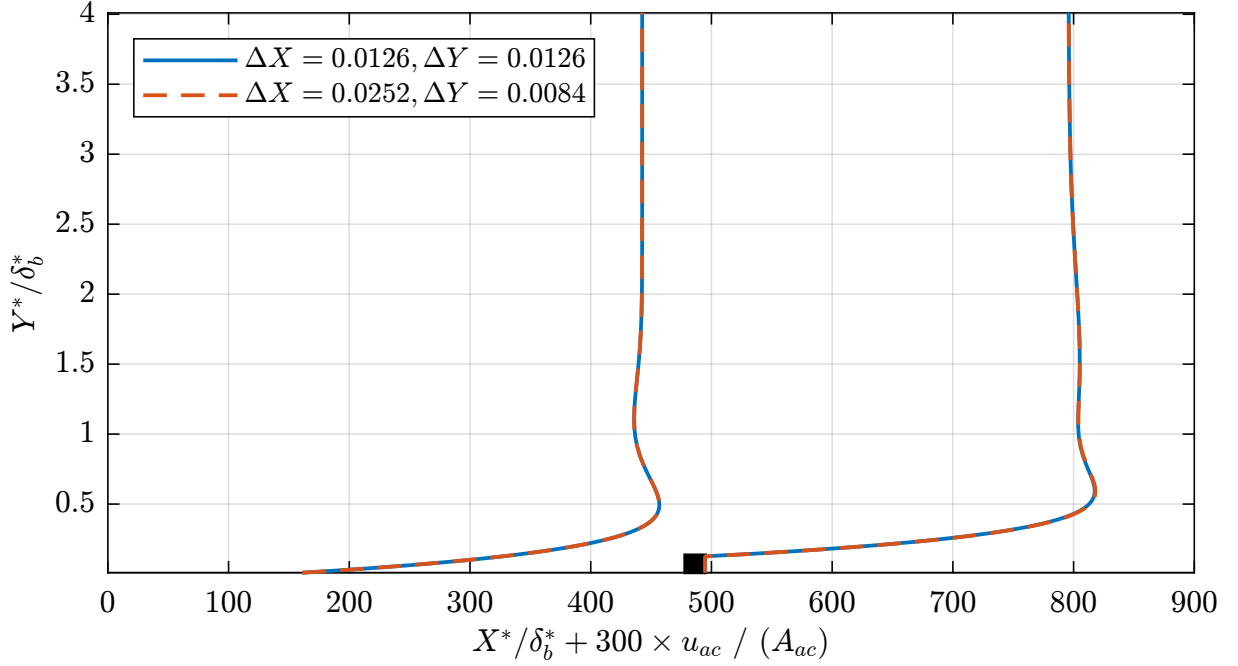
Figure 9 – Stokes Layer profile measured on the rough flat plate (bump) at different streamwise positions for different mesh refinements. The stokes layer profile is multiplied by 300 to improve the graphical readability. The curves overlap.
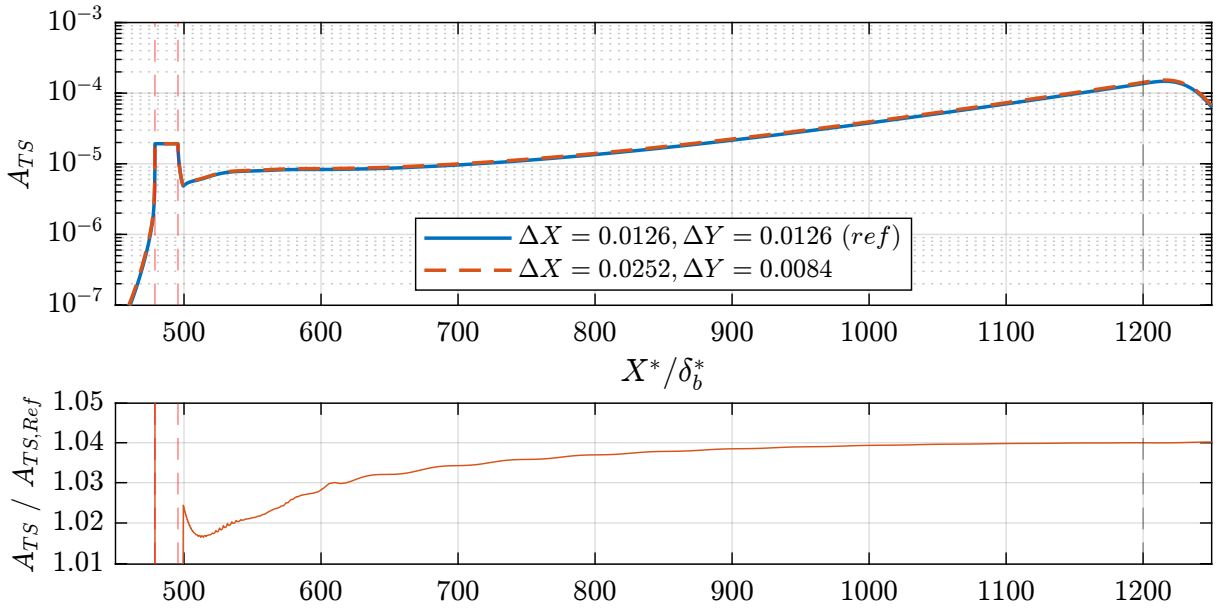
Figure 10 – TS wave generated by acoustic receptivity with different mesh refinements. The top figure is the TS evolution, and the bottom figure is the ratio between the evolutions.

wave over the smooth plate with Mach 0.1 and 0.2. The bottom chart shows that the difference is approximately 4% over the plate, which is in accordance with the numerical precision discussed before. Furthermore, as the experimental study of Placidi, Gaster and Atkin (2020) was conducted at Mach 0.05, approximately, the difference between the evolution of the experimental TS wave and the simulated one, if other physical parameters
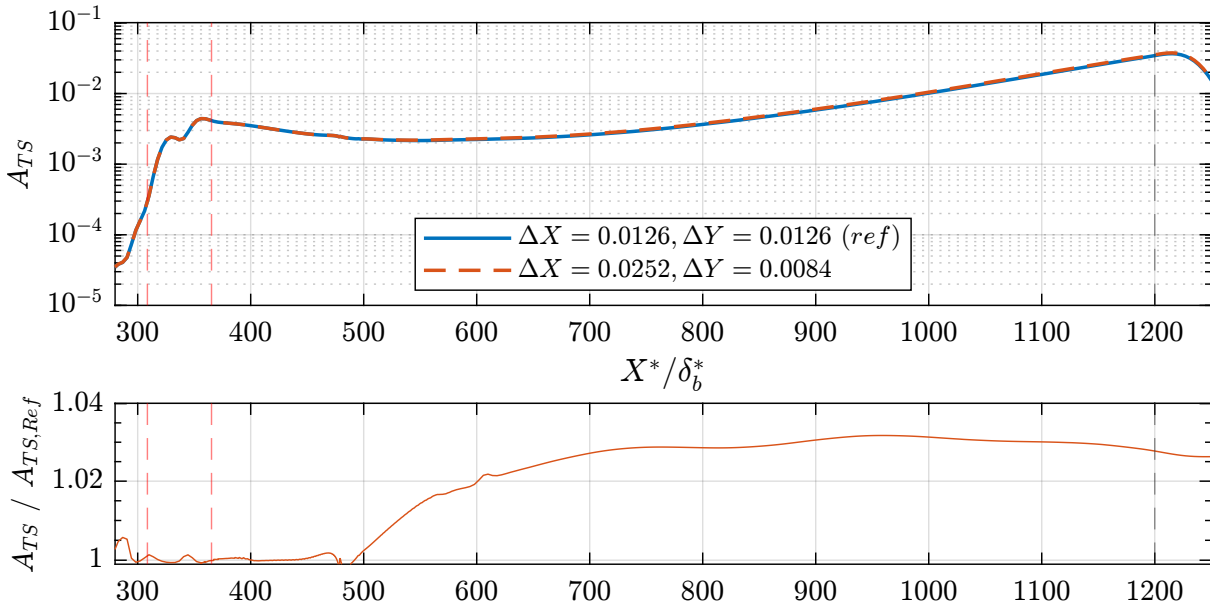
Figure 11 – TS wave generated by suction and blowing on the wall with different mesh refinements. The top figure is the TS evolution, and the bottom figure is the ratio between the evolutions.

are equal, is thought to also be within 4%.
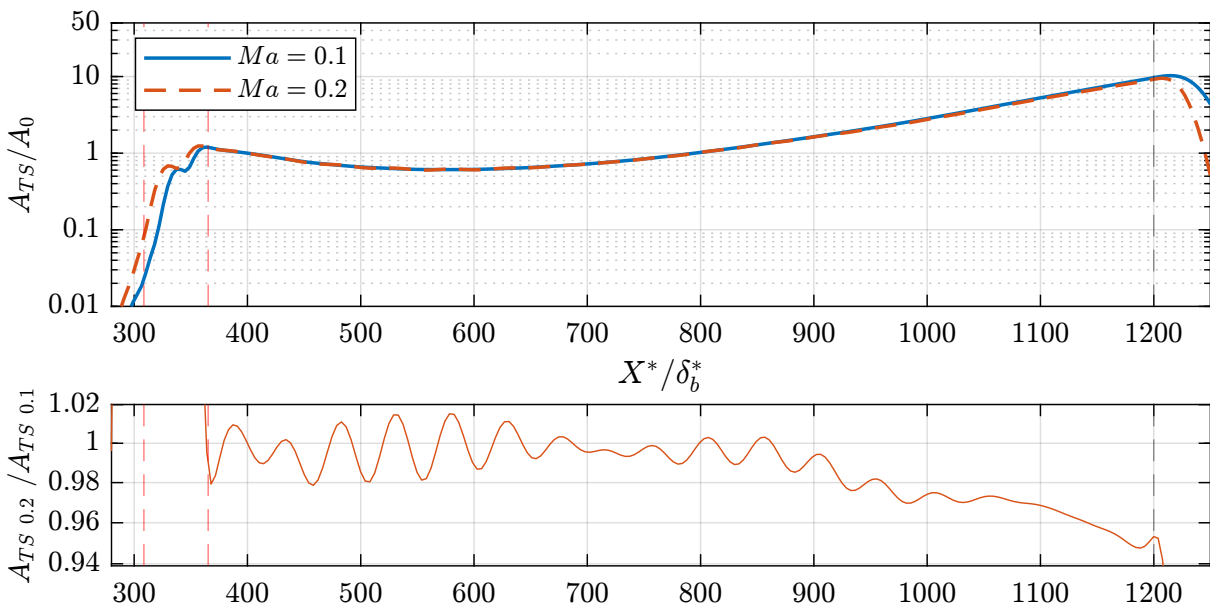
Figure 12 – Top: TS wave (A_{TS}) generated by suction and blowing at the wall for Ma = 0.1 and 0.2 divided by the respective amplitudes at first branch (A_0). Bottom: ratio between the TS wave amplitudes at Ma = 0.2 ($A_{TS\ 0.2}$) and 0.1 ($A_{TS\ 0.1}$).

5 PRELIMINARY RESULTS AND VALIDATION

5.1 Characteristics of the acoustic receptivity due to a sharp bump

The receptivity characteristics simulated in the present parameter space are addressed before any comparison with the data from the literature as previous receptivity studies have yet to deal with the non-linearity of the phenomenon concerning the roughness height. It is necessary to standardize the initial amplitude measurement considering this non-linearity.

Figure 13a presents the evolution of a TS wave introduced by acoustic receptivity due to a rectangular bump of height 33.6% of δ_b^* ($TS_{receptivity}$). It also presents two TS waves generated by suction and blowing at the wall passing over the same rectangular bump (TS_{rough}) and over a smooth wall (TS_{smooth}). On one hand, the amplitude of the TS_{rough} was adjusted to match the $TS_{receptivity}$ at a downstream position. On the other hand, the amplitude of the TS_{smooth} was adjusted to match the amplitude of the TS_{rough} at an upstream position.

The $TS_{receptivity}$ presents a region of significant amplification in the near field downstream of the roughness and matches the TS_{rough} at a certain point. The extent of this region might depend non-linearly on the roughness height, as it will be discussed in the following sections; this may need to be properly accounted for in linear calculations.

The ratio between the TS_{rough} and TS_{smooth} is also plotted in Figure 13b. It shows that after a certain position downstream ($X^*/\delta_b^* > 650$), the growth rate is similar, which suggests that any non-linear effect might be confined to a limited region near the roughness.

Fig. 14 shows the contour lines of iso values of the TS wave over the flat plate in the cases of TS_{rough}, TS_{smooth} and $TS_{receptivity}$. Moreover, Fig. 15 presents the evolution of the integrated kinetic energy along the normal direction. It is possible to notice that the roughness has a negligible effect on the stability upstream of the roughness.

However, in the roughness' near field, the TS_{rough} suffers an increase and a following decrease in the amplitude, and it approximately matches the amplitude of the TS_{smooth} at the trailing edge position of the roughness. Moreover, the amplitude of the TS_{rough} increases compared to the TS_{smooth} at downstream positions. This behaviour is believed to be due to the interaction with the roughness, as discussed by Himeno et al. (personal communication).

The method utilized in some previous studies, such as Würz *et al.* (2003b), to evaluate the initial amplitude of the TS wave from receptivity is to match the amplitude of the TS_{rough} with the amplitude of the $TS_{receptivity}$ at a certain downstream position and
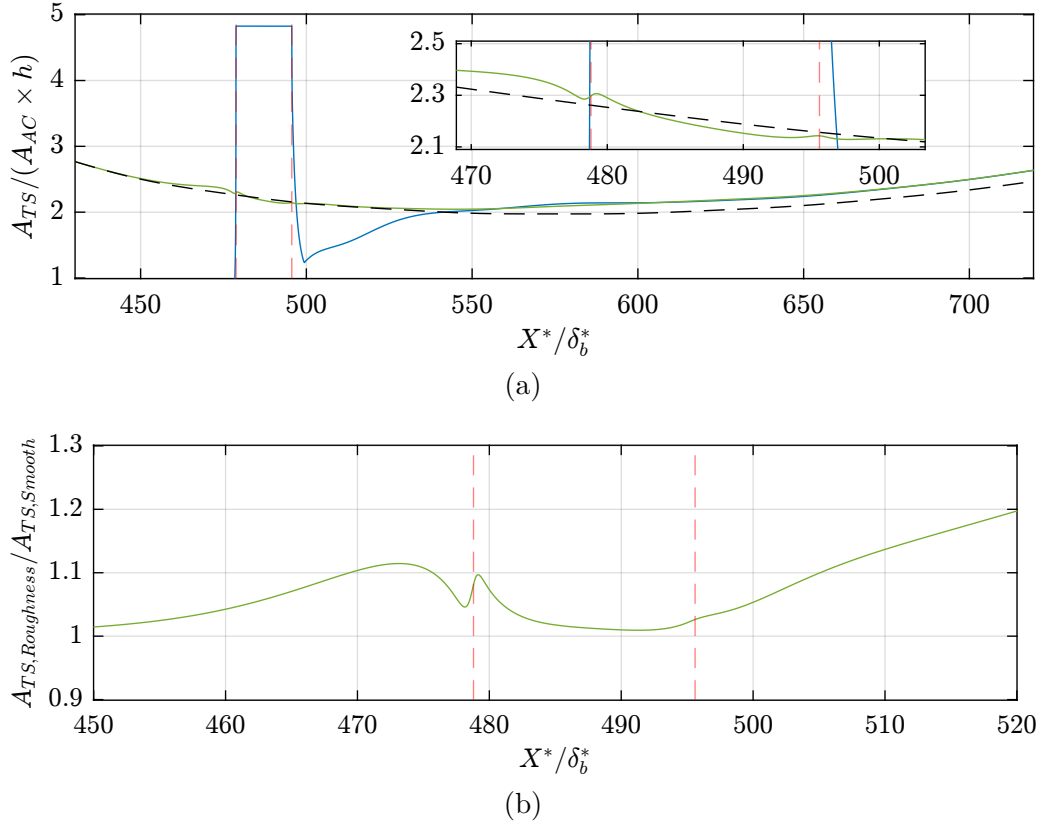
Figure 13 – Top: The blue solid line is the evolution of the maximum of a TS wave (A_{TS}) generated by acoustic receptivity due to a rectangular bump of height $h/\delta_b^* = 33.6\%$, normalized by the roughness height and the acoustic wave amplitude (A_{ac}). The figure also presents the maximum of a TS wave generated by suction and blowing at the wall passing over the same rectangular bump (solid green) and the maximum of a TS wave generated by suction and blowing at the wall passing over a smooth wall (black dashed). Bottom: ratio between the TS wave passing over the rough surface ($A_{TS,Roughness}$) and the TS wave passing over the smooth surface ($A_{TS,Smooth}$).

evaluate this adjusted amplitude at the center of the roughness. However, one can argue that the amplitude of the TS_{rough} varies abruptly depending on the roughness position. This variation could lead to less precision in evaluating the initial TS amplitude.

A potentially more robust alternative method to measure the initial amplitude is first to match the TS_{rough} amplitude with the $TS_{receptivity}$ at a downstream position, and secondly to match the TS_{smooth} with the amplitude of the TS_{rough} at an upstream position and then evaluate this adjusted amplitude at the desired position (e.g., the center of the roughness or the trailing edge of the roughness). This method is potentially more robust than the method utilized in previous works because the evolution of TS_{smooth} does not present abrupt changes. Moreover, as the upstream matching region is unaffected by the roughness, this procedure allows to distinguish the amplitude due to the receptivity itself and the amplitude due to the TS wave passing over the near-field of the roughness element.
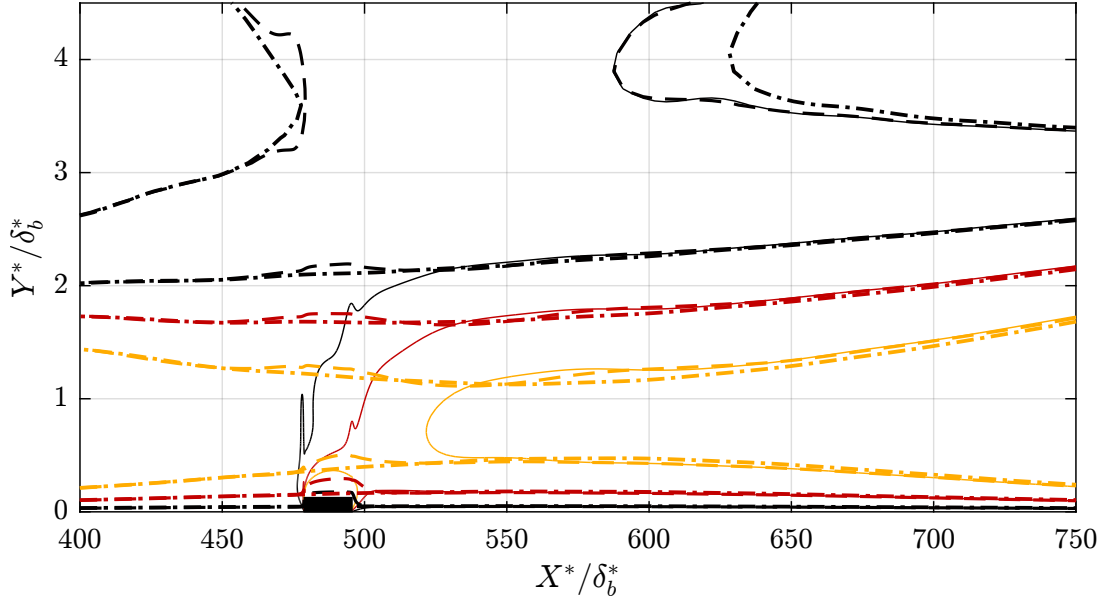
Figure 14 – Contour lines of different levels of the TS wave over the smooth surface (dotted-dashed), over the rough surface with $h/\delta_b^* = 12.6\%$(dashed), and the TS wave from acoustic receptivity (solid). The black rectangle is the roughness. The curves were normalized with the procedure described in section 5.1.
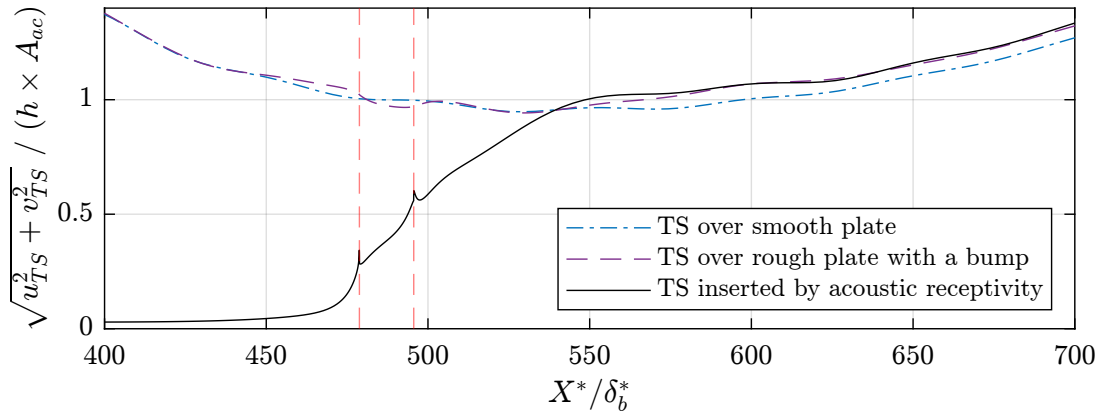
Figure 15 – Evolution of the integrated kinetic energy of the TS wave along the normal direction passing over the flat plate with the hump with $h/\delta_b^* = 12.6\%$, over the smooth surface, and the TS wave from acoustic receptivity (solid blue line). The red dashed lines delimit the hump position in both figures. The curves were normalized with the procedure described in section 5.1. It also suggests that there is no influence of the roughness upstream of the rectangular element, and the evolution of the receptivity wave and the TS over the rough surface is similar downstream of the roughness element.

Although the difference between the amplification of the TS passing over the smooth and the rough surface for roughness with small heights may be negligible, as it is demonstrated in Fig. 16, in the case of higher heights, such as the heights simulated herein, the difference between the procedure described in this work and the procedure from Wörner, Rist and Wagner (2003) is significant. Thus, this method was utilized henceforth.

It is also worth noting that the dependency of the receptivity with respect to the acoustic wave amplitude was found to be linear within the range of magnitude tested herein. This behavior can be seen in Fig. 17, where the Stokes Layer profile at a downstream position with respect to the roughness divided by the acoustic wave amplitude at the freestream for different acoustic wave amplitude overlap. It also shows that negligible TS waves remain in this position due to the leading edge receptivity because the profile does not change.

The same behaviour is observed in Fig. 18, where the receptivity amplitude for different roughness heights is plotted against different acoustic wave amplitude. Again, it is possible to see linear trends among the receptivity of each roughness height, but with different derivatives.

This linear dependence is somewhat different from what Saric (1994) observed in its experimental results. The explanation given by Nayfeh and Ashour (1994) for the results presented in Saric (1994) indicated that some TS wave might remain from the leading edge receptivity in the roughness area, which is not the case in the present simulation, as discussed in the previous paragraphs. So, the TS wave observed in this simulation is thought to be mainly due to roughness, and the Figs. 17 and 18 reinforce the findings of Nayfeh and Ashour (1994).

At last, it was also found that the vertical TS disturbance velocity component could be obtained from the single numerical simulation of the acoustic streamwise wave passing over the roughness. This vertical component's evolution parallels the streamwise disturbance component obtained by the subtraction technique explained in sec. 3.1, as it is shown in Fig. 19. Using this vertical component would eliminate a number of simulations required. Notwithstanding, the subtraction technique was utilized in this work to compare with experimental results.

5.2 Comparison with others numerical simulations

In figure 20, the simulation data was compared with the numerical data of Würz *et al.* (2003b) and the data from the Finite Reynold Number Theory presented in Choudhari and Streett (1992). This comparison utilized the efficiency function Λ_u as described by Choudhari and Streett (1992), which is a normalization of the maximum amplitude of the TS wave at the center of the roughness with respect to the Fourier transform of the

shape of the roughness itself and the acoustic wave amplitude. The results present a good agreement. However, the current DNS seems to agree slightly more with the theory than the numerical data of Würz *et al.* (2003b).

5.3 Comparison with experimental data

After the validation with theoretical and numerical data, the present DNS simulation is compared with the experimental data from Placidi, Gaster and Atkin (2020). Thus, figure 21 shows the experimental TS wave profile at a downstream position (Fig. 4b in Placidi's paper) and the simulated profile at the same flow conditions reported in his paper, with exception of the Mach number, which was discussed in section 4.4. It is possible to note that the experimental TS wave profile has a similar shape to the simulated one. However, the amplitude is greater by a factor of 1.2, which is thought to be larger than the simulation uncertainty.

One possible explanation for this difference might be the effect of the pressure gradient over the flat plate in the TS wave evolution. Thus, Figure 22a presents an estimated Falkner-Skan-Coke profile (FSC) with pressure gradient based on the experimental data present in Fig. 2.1 of Veerasamy (2019), which is cited by the authors of Placidi, Gaster and Atkin (2020) as a typical accuracy achieved in their facility. Next, Figure 22b compares the evolution of the TS wave with and without the estimated pressure gradient. One can see that even a mild pressure gradient of m = -0.0015 has an impact of about 20% in the amplitude in the experimental measurement region ($X/\delta^* \approx 1100$), which could explain the difference observed between the numerical and experimental results. It shows how difficult it is to perform this experiment.

In order to compensate for this difference in the downstream TS amplitude, the data from the simulation will be multiplied by a factor for positive heights and another factor for negative heights in order to match the theoretical data presented in Placidi's paper for the lowest roughness height simulated (positive or negative). This correction will be detailed in the following sections.
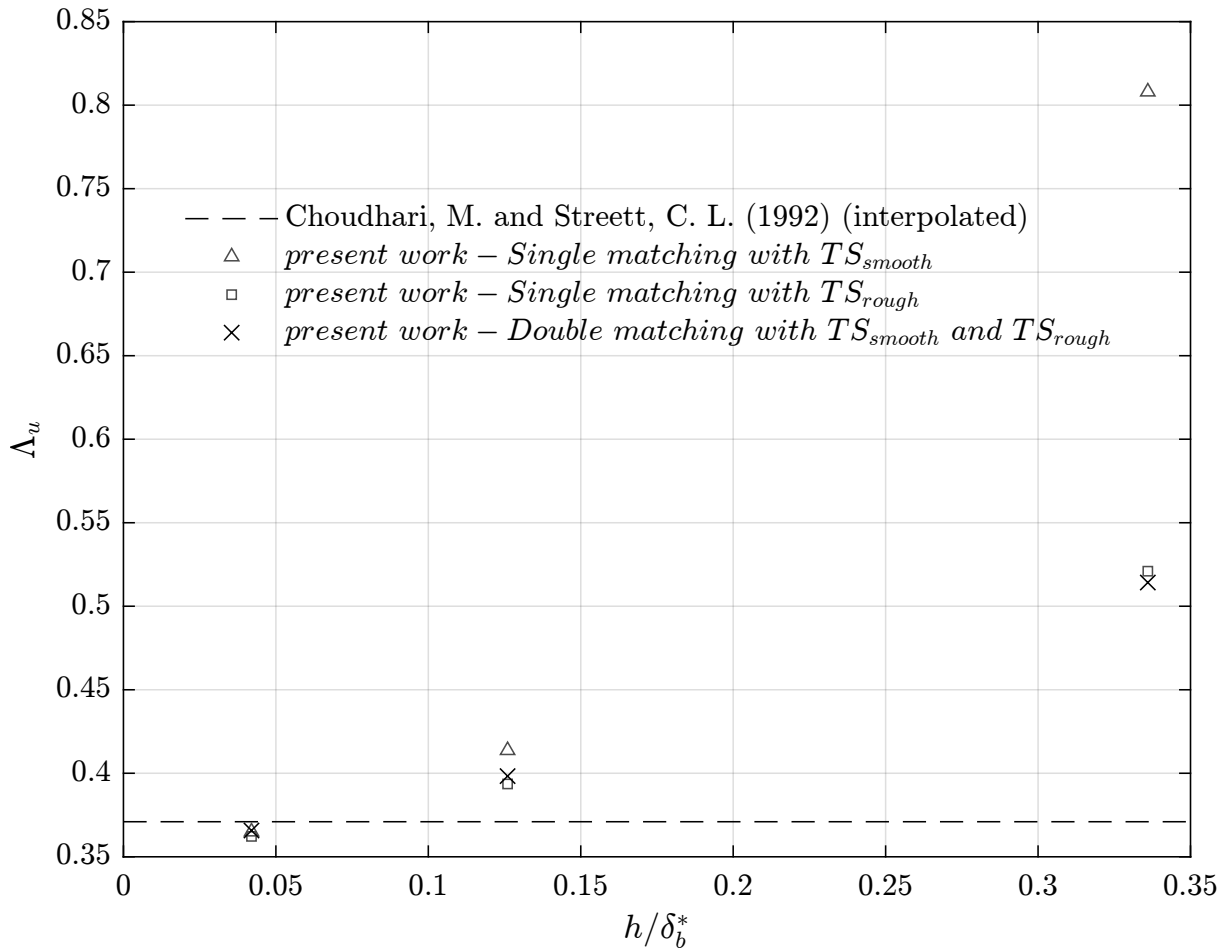
Figure 16 – Efficiency function (Λ_u) defined in Eq. 20 in Choudari, M. and Streett, C. L. (1992) for $R = \sqrt{Ux/\nu} = 829.6$. Comparison among different methods for acoustic receptivity measurement at the roughness position. Ma is 0.1.
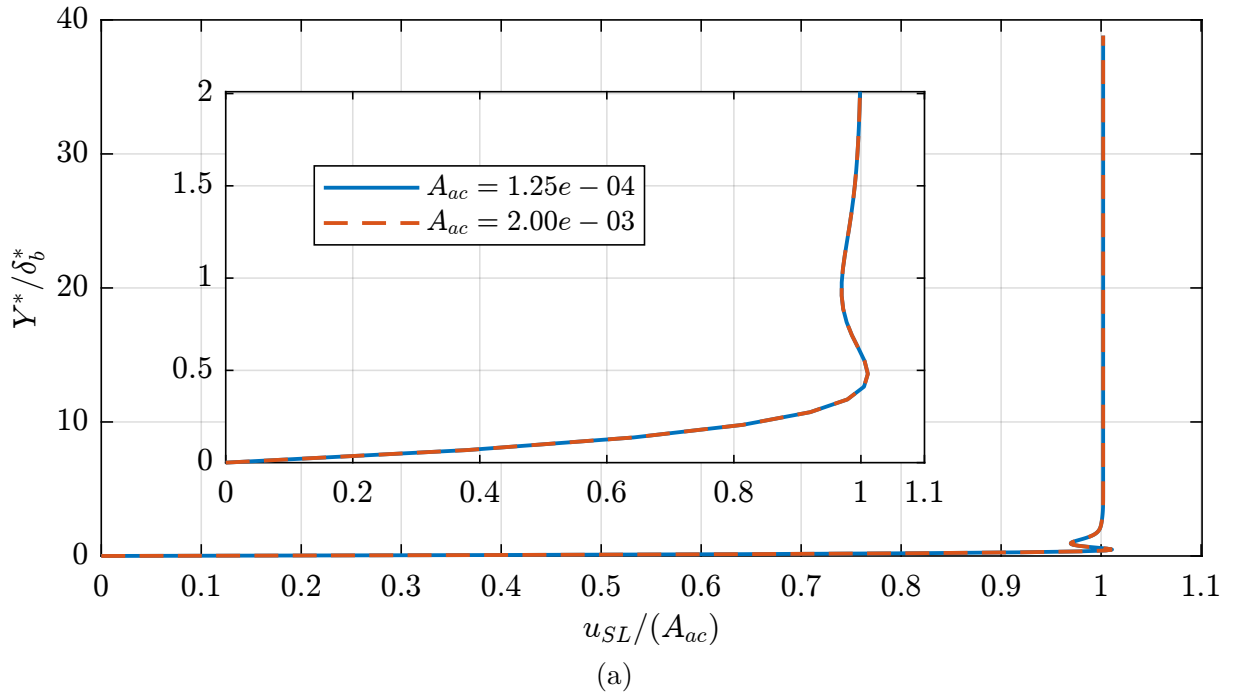
Figure 17 – Stokes Layer profile (u_{SL}) at a downstream position divided by the acoustic wave amplitude at the free-stream. The curves overlap.
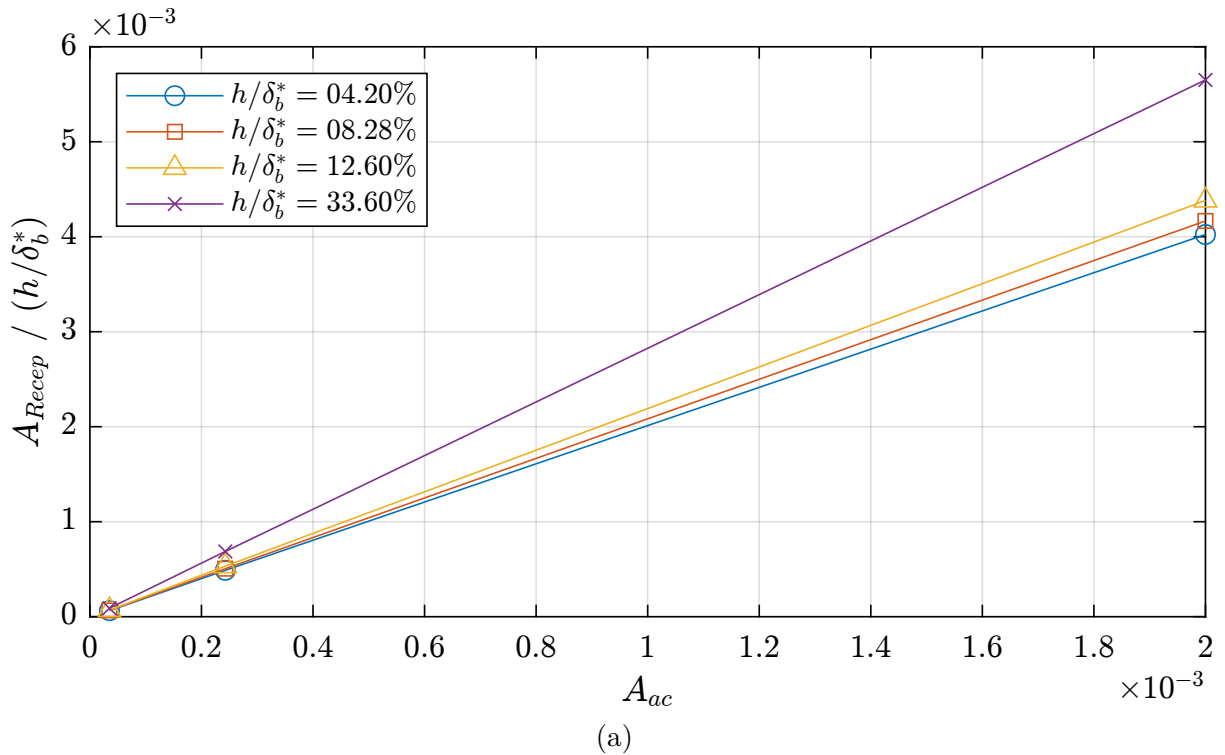
Figure 18 – Receptivity amplitude measure using the procedure described in Sec. 5.1 for different roughness heights and acoustic wave amplitudes.
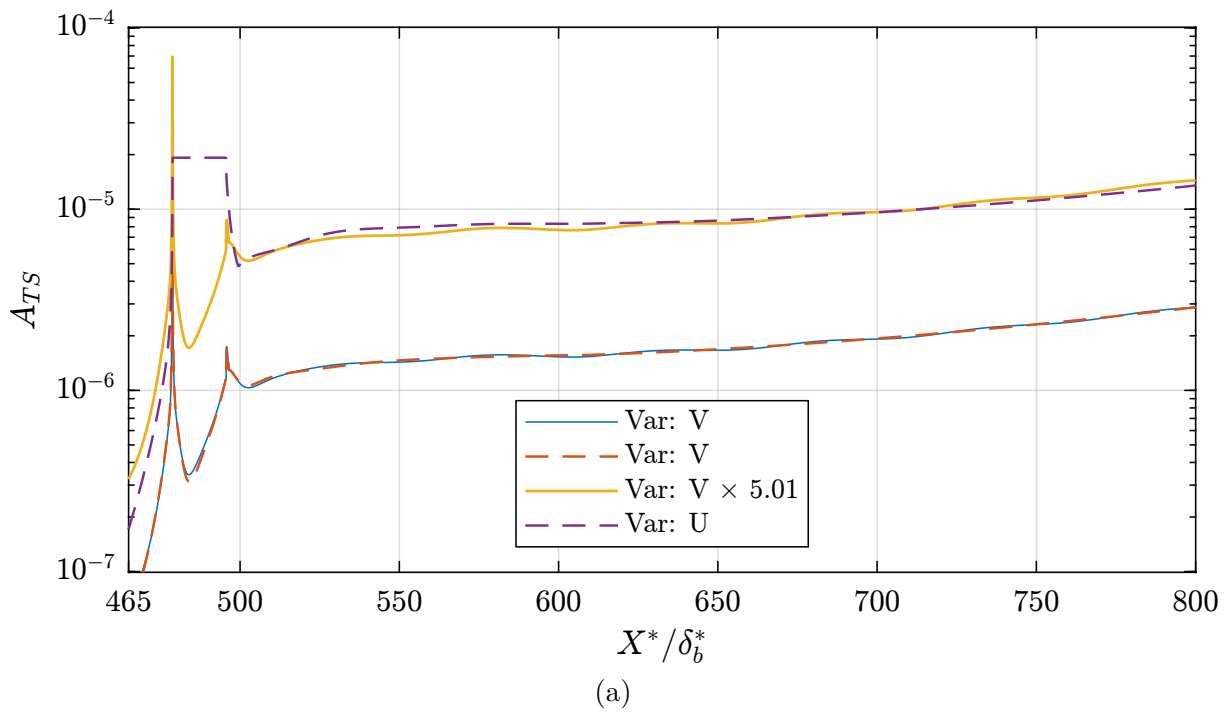
Figure 19 – Comparison between the maximum of a TS wave inserted by the acoustic receptivity of a bump with $h/\delta_b^* = 12.6\%$ obtained by the subtraction technique described in Sec. 3.1 (dashed) and by the vertical component of the single case of the acoustic wave passing over the roughness (solid).
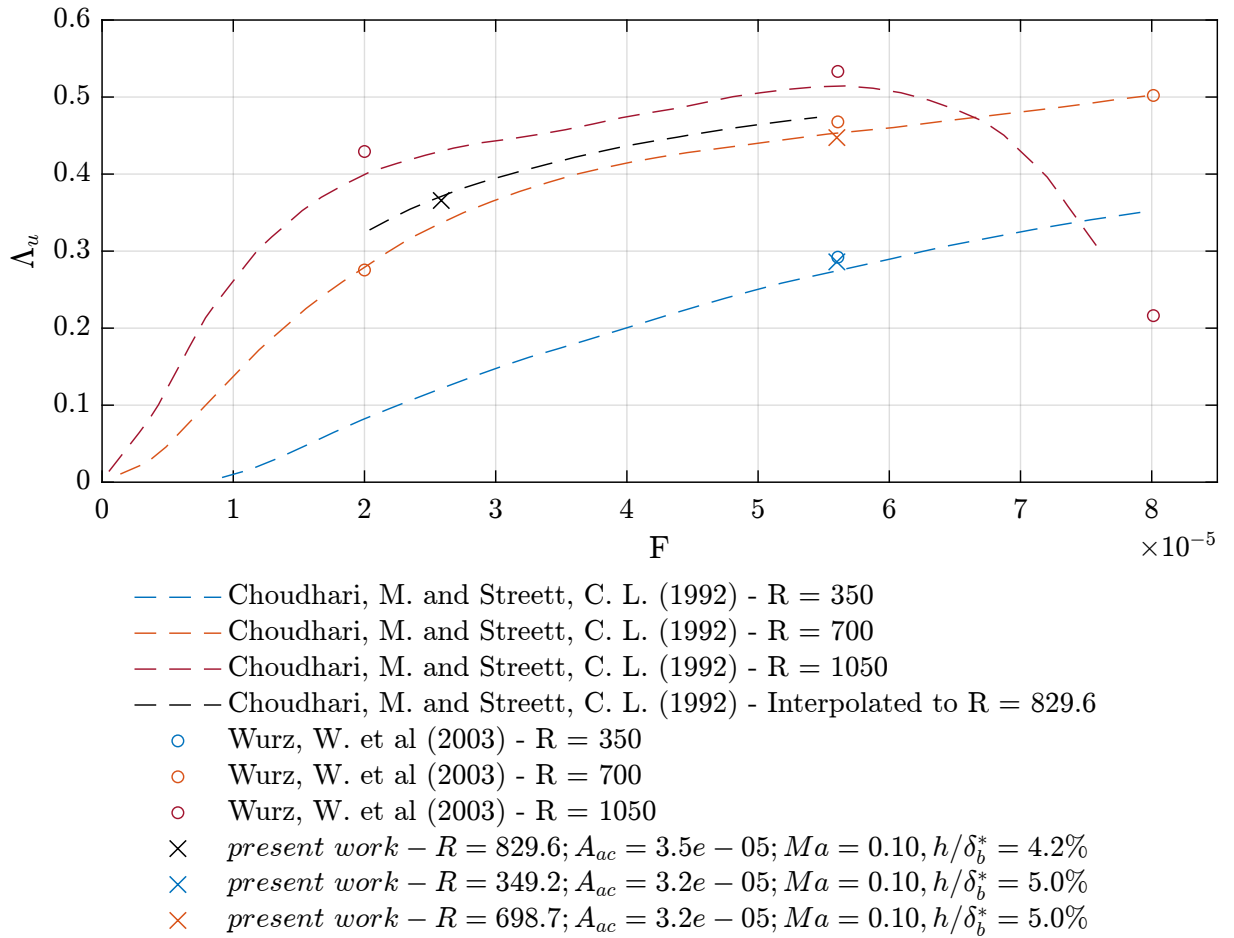
Figure 20 – Efficiency function (Λ_u) defined in Eq. 20 in Choudari, M. and Streett, C. L. (1992) evaluated at different Reynolds number based on streamwise position ($R = \sqrt{Ux/\nu}$). Comparison with the numerical work of Wurz, W. et al. (2003) and the theoretical results of Choudari, M., and Streett, C. L. (1992).
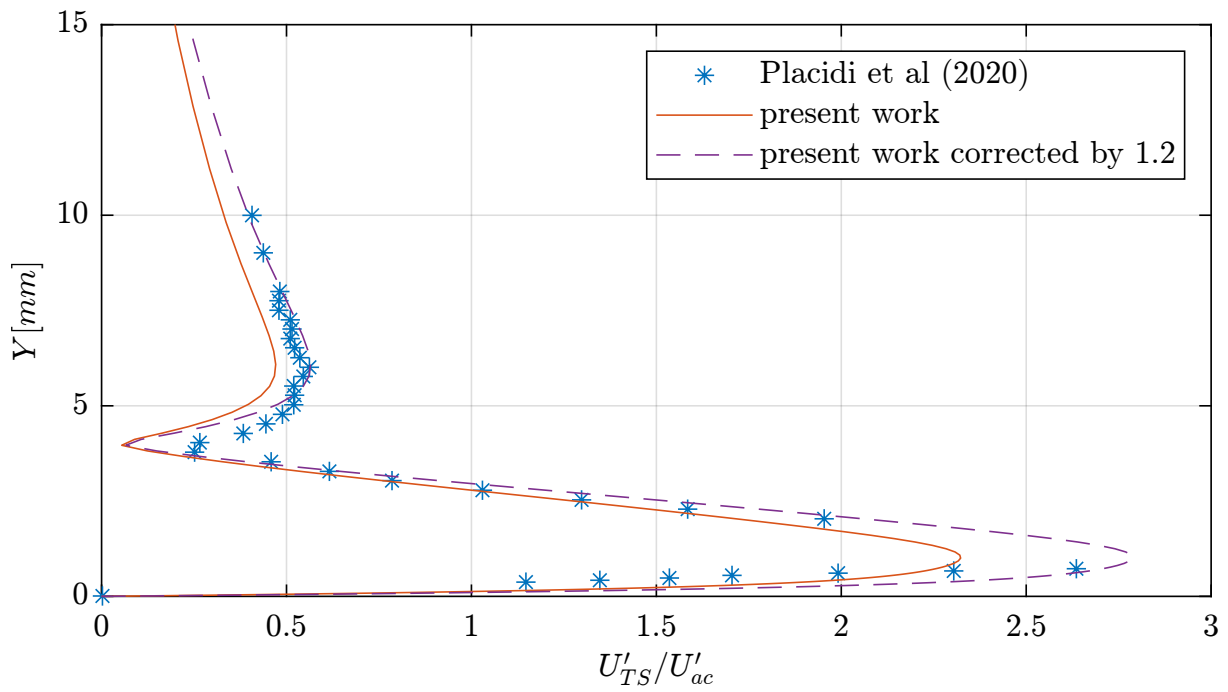
Figure 21 – TS profile comparison between the present work (solid orange) and the data present in figure 4b of Placidi et al. (2020) (blue symbols). The present data is corrected by 1.2 (purple dashed) to overlap the experimental data.
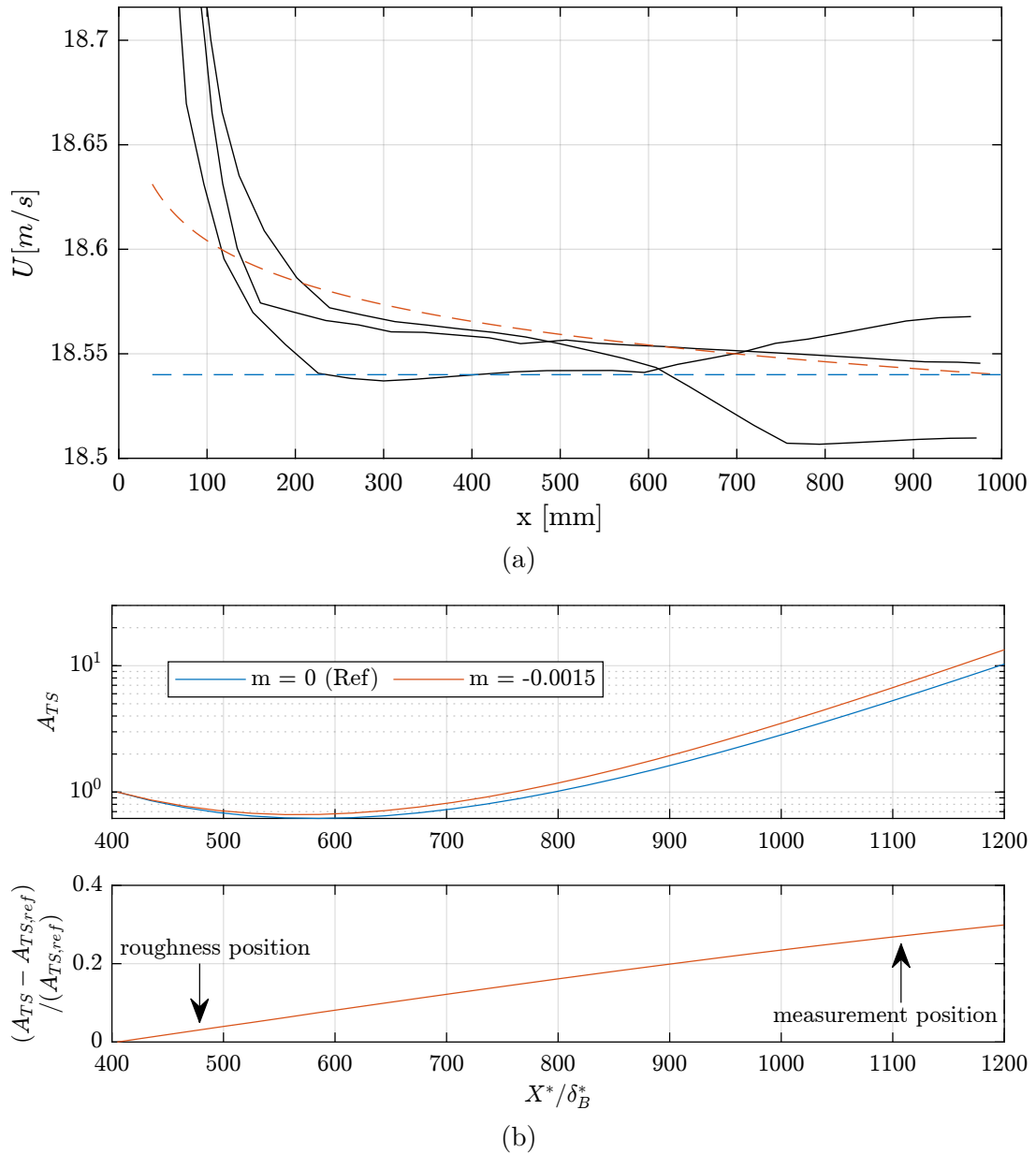
Figure 22 – a) Estimated outerflow velocity (black solid lines) and Falkner-Skan-Coke profiles envelope (dashed lines) with m = 0 (blue) and m = -0.0015 (red). b) Top: TS wave evolution calculated with the PSE algorithm over a flat plate with the "m" parameter from the Falkner-Skan-Coke envelope of (a) (m = 0 and -0.0015). Bottom: ratio between the TS wave amplitude from the top figure.

6 PARAMETRIC STUDY OF RECEPTIVITY

6.1 Roughness height effect

This section assesses the effect of varying the positive roughness height. Firstly, the experimental data of Placidi, Gaster and Atkin (2020) is compared to the simulation data. Next, the non-linearity of the receptivity is assessed, and this provides a suggestion for the difference encountered with the experimental data.

6.1.1 Comparison with experimental data

Figure 23 shows the maximum of the TS wave amplitude from acoustic receptivity of humps at $X^*/\delta_b^* = 1108.8$ divided by the free-stream acoustic wave amplitude. It compares the experimental data of Placidi et al., the linearised simulation data in Placidi's paper, and the present DNS simulation. The experimental and the linearised simulation data were adjusted in the X-axis by the displacement thickness based on Blasius at the hump position. The present DNS simulation data was adjusted in the Y axis to match the linearised simulation at the lowest height available.

From this figure, one can note that the simulation data has a departure from the linear for $h/\delta^* = 12.6\%$ behaviour that was not predicted by the linearised simulation. As was pointed out in section 5.1, the observed non-linearity might come from the combination of the near-field effect on the evolution of the TS wave and the non-linearity of the receptivity itself.

6.1.2 Non-linearity with respect to the bump height due to receptivity

As discussed before, part of TS from receptivity is due to the interaction of the TS wave passing over the near-field of the roughness. So, Fig. 24 presents the evolution of a TS generated by suction and blowing at the wall passing over the smooth surface and the rough surface with different bump heights. The amplitude is divided by the height of the bump, and the lines do not collapse, which suggests non-linearity in the evolution of the TS with respect to the roughness height.

The effect of the near field of the roughness on the evolution of the TS wave is treated in Himeno et al. (personal communication). Here, their comparison of the growth rate change, α, is reproduced to determine the X station where the roughness effect has cessed. It is worth pointing out that this distance does not increase with the roughness height, but the amplitude of the disturbance and the growth rate do.

The TS amplitude from receptivity is plotted in Fig. 26 along with the TS wave over the smooth and rough surface. The normalization procedure is described in section 4.1.
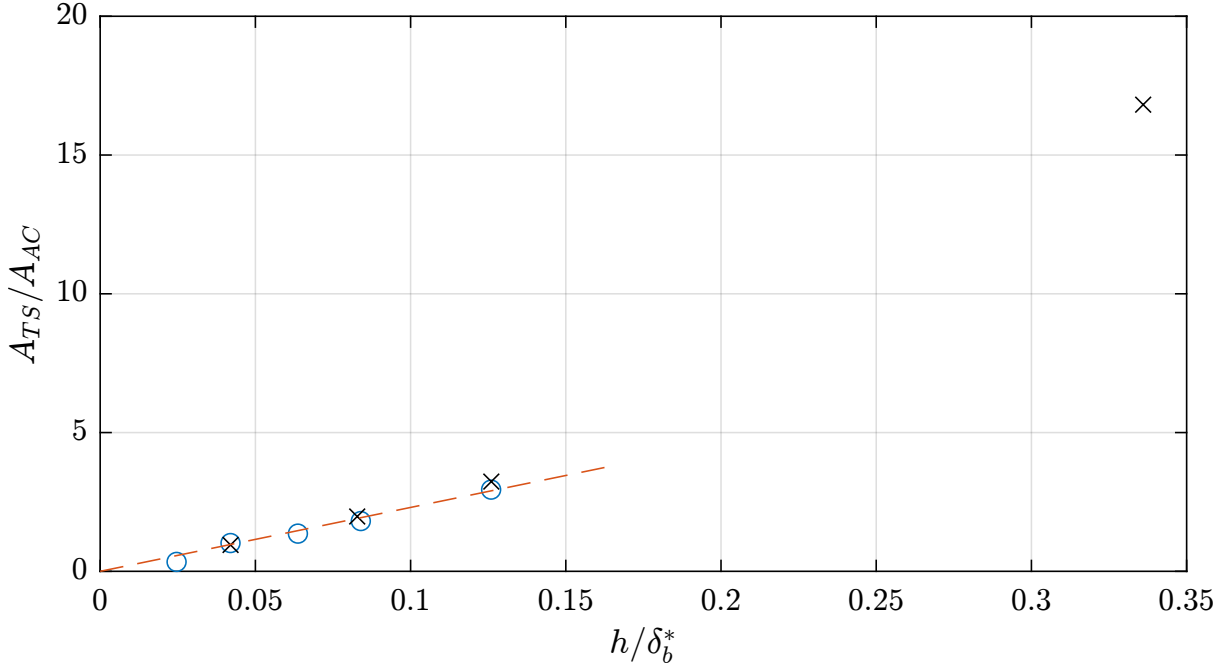
Figure 23 – Maximum of the TS amplitude from acoustic receptivity of humps at $X^*/\delta_b^* = 1108.8$ divided by the freestream acoustic wave amplitude. Comparison among the experimental data of Placidi, Gaster and Atkin (2020) (circles), the linearised simulation data present in Placidi's paper (dashed line), and the present DNS simulation (cross). The present simulation was corrected to match the lowest height from the experiment.

The position of the downstream matching was chosen to be where the disturbance wave has the same TS growth ratio, as depicted in Fig. 25. As the lines do not collapse in Fig. 26, the results suggest the presence of non-linearity at the heights simulated. This result also suggests that the non-linearity of the receptivity (measured by the difference of the dashed lines) is somewhat more significant than the non-linearity due to the interaction of the TS passing over the near-field of the roughness (measured by the difference between the green line and the respective dashed line).

6.2   Gap depth effect

In this chapter, the effect of varying the gap depth is assessed. As done in the previous chapter, the experimental data of Placidi, Gaster and Atkin (2020) is compared to the simulation data, and then the non-linearity of the receptivity is studied.

6.2.1   Comparison with experimental data

Figure 27 shows the maximum of the TS wave amplitude from the acoustic receptivity of the cavity at $X^*/\delta_b^* = 1108.8$ divided by the free-stream acoustic wave amplitude. It also compares the experimental data of Placidi, Gaster and Atkin (2020), the linearised simulation data in Placidi's paper, and the present DNS simulation. Similarly, as before,
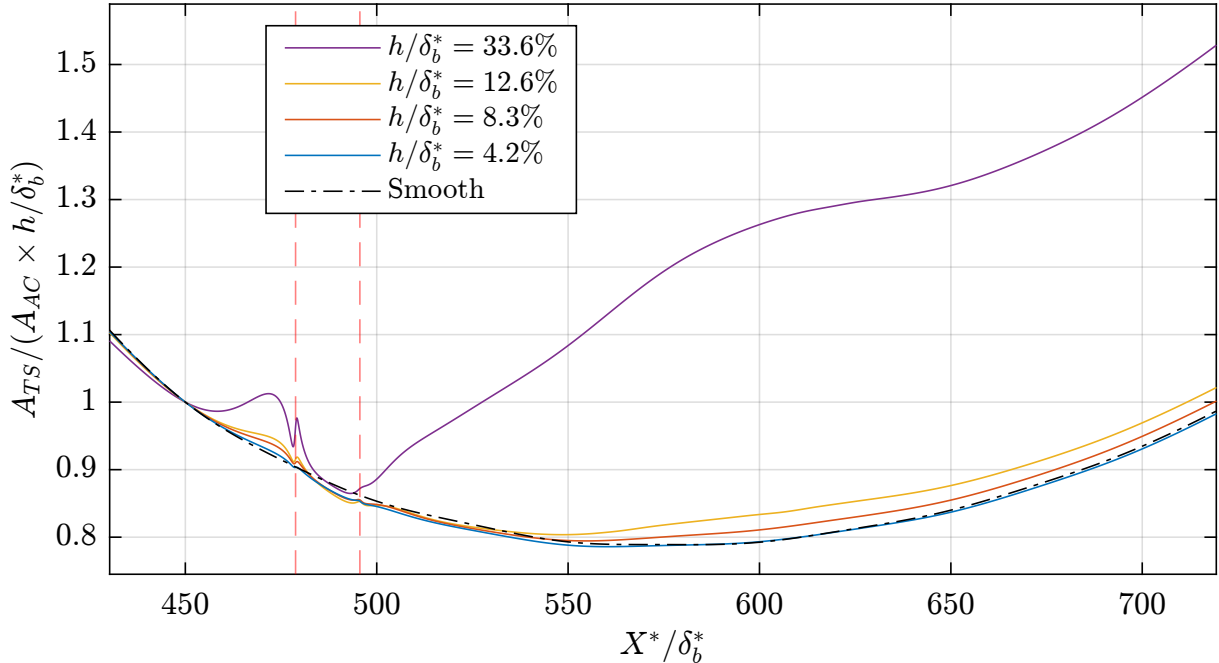
Figure 24 – Amplitude of TS waves passing over the smooth surface and rough surface with a localized rectangular bump.

the experimental and the linearised simulation data were adjusted in the X-axis. Likewise, the DNS simulation data was adjusted in the Y-axis to match the linearised simulation at the lowest height.

The cavity simulation data presented a departure from the linear behavior weaker than the hump. Meanwhile, the experimental data presented a departure from the linear behavior in heights smaller than these predicted in the simulations. This behavior was argued by Placidi et al. (2020) as an effect of a possible bubble formation inside the cavity. However, the DNS simulations did not present the same pattern, and a lack of precision in the experimental measurement for the small heights may cause this discrepancy.

Also, the observed non-linearity might come from the combination of the near-field effect on the evolution of the TS wave and the non-linearity of the receptivity itself.

6.2.2 Non-linearity with respect to the gap depth due to receptivity

Similarly, in the hump case, Fig. 28 presents the evolution of a TS generated by suction and blowing at the wall passing over the smooth surface and the rough surface with different cavity heights. The amplitude is also divided by the height of the cavity, and the lines do not collapse, which suggests non-linearity in the evolution of the TS with respect to the gap depth.

The growth rate caused by the gap is plotted in Fig. 29. It shows that in a position downstream near $X^*/\delta_b^* = 530$, the effect of the cavity has cessed. This position was utilized to adjust the amplitude of the $TS_{roughness}$.
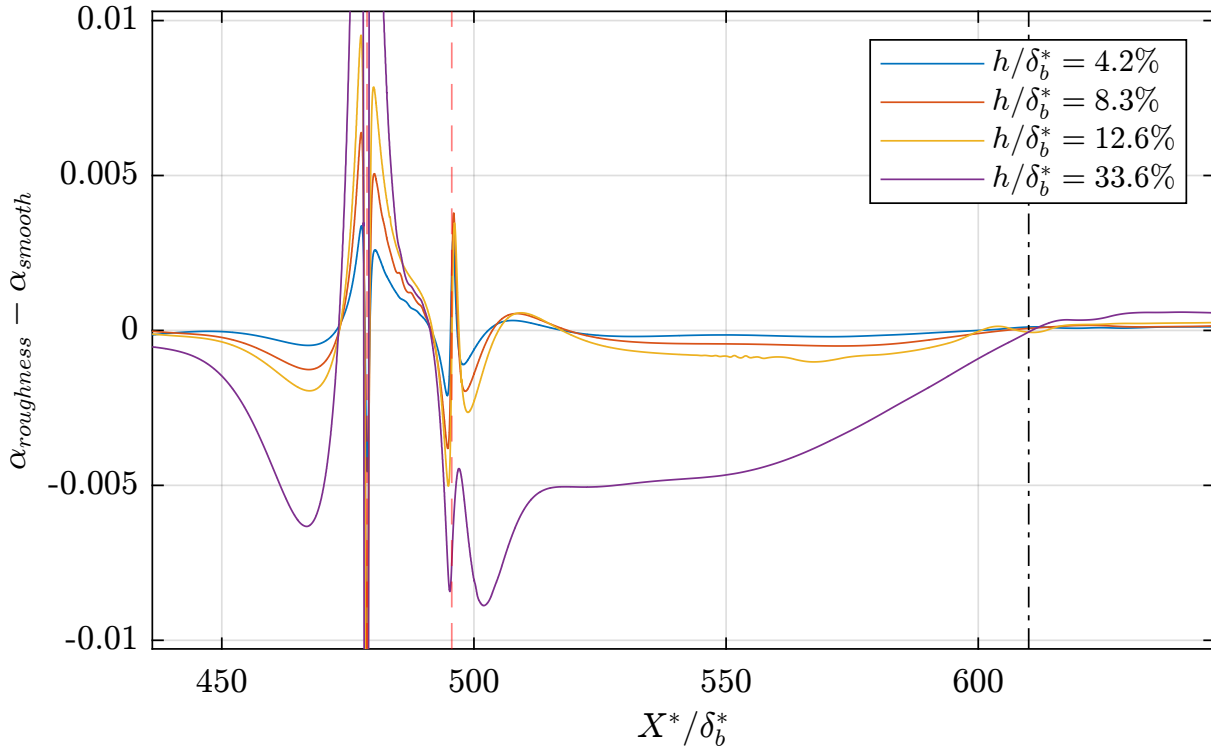
Figure 25 – Disturbance in the growth rate (α) between the cases with and without bump.

Fig 30 presents the amplitude of the TS wave from receptivity and the evolution of the TS wave over the smooth and rough surface. The normalization procedure is described in section 5.1. Differently from the hump case, in this gap case, the black dashed lines approximately collapse, which suggests that the receptivity of acoustic waves over cavities is linear to the cavity height, at least for the heights simulated in this work.

6.3 Comparison between receptivity of bumps and cavities

In order to compare the receptivity of humps and cavities of the same heights, Fig. 31 presents the amplitude measured in the middle of the roughness position utilizing the procedure described in section 5.1. It is possible to see that the initial amplitude of bumps is consistently greater than the cavities'. Moreover, the cavity receptivity seems to be linear with the roughness height, and the receptivity of the bump does not vary linearly.

6.4 Mach number effect

This section assesses the effect of varying the Mach number on the receptivity. Fig. 32 presents the difference of the growth rate of a TS generated by suction and blowing at the wall with and without a bump of height $h/\delta_b^* = 12.6\%$. Near $X^*/\delta_b^* = 640$, the growth rate disturbances are minimal, so this position was chosen to match the TS_{rough} to the $TS_{receptivity}$.

Figure 33 shows the evolution of the $TS_{receptivity}$, and their respective TS_{rough} and
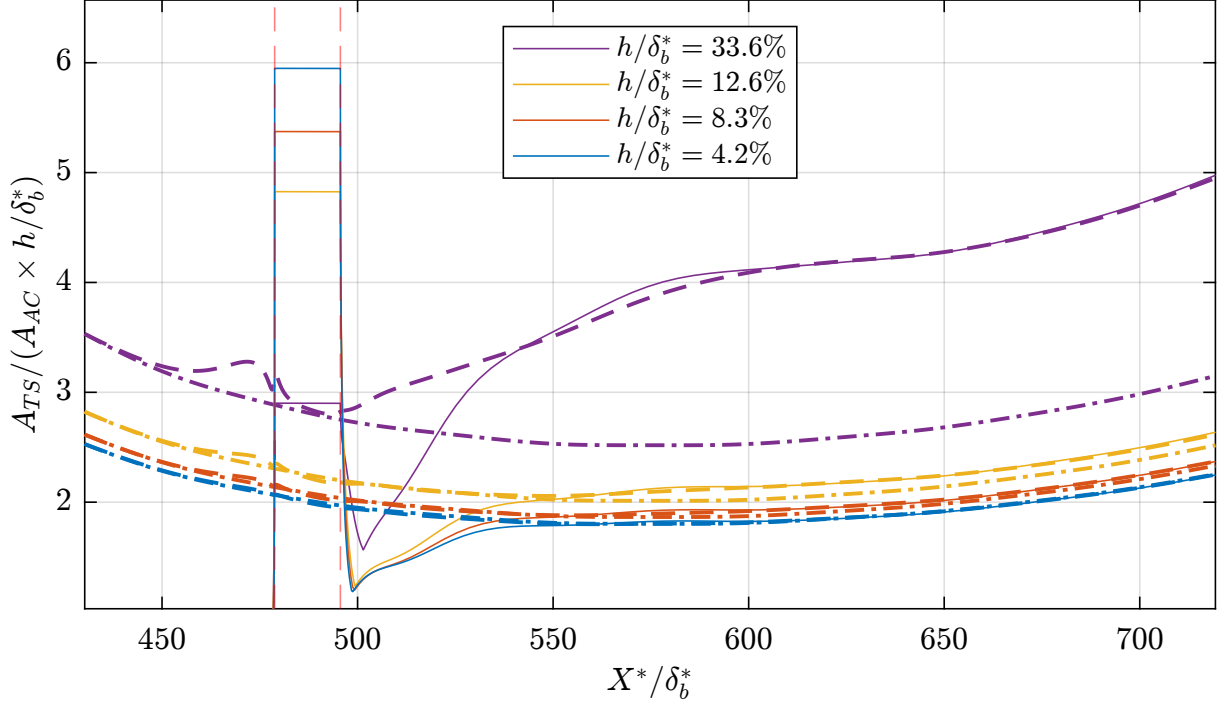
Figure 26 – Comparison among the maximum of the TS amplitude generated by acoustic receptivity for different bump heights normalized by the acoustic wave amplitude and the roughness height (solid lines). This figure also presents the normalized maximum amplitude of the TS passing over the roughness (dashed) and the normalized maximum amplitude of the TS passing over the smooth plate (dash-dotted).

TS_{smooth}. Unlike the previous cases, the evolution of the TS waves inserted by suction and blowing at the wall presented a more wavy pattern. This pattern is due to the acoustic admittance, which increases with the Mach number. There, the signal of the Fourier transform is noisier, and the results seem to be more wavy-like. However, this waviness was considered small enough to measure the receptivity at the center of the roughness.

Figure 34 presents the receptivity coefficient measured following the procedure described in section 4.1 for different Mach numbers. The data suggests that the receptivity decreases with the Mach number, which is somewhat similar to the results presented in Fig. 5c of Raposo et al. (2019).
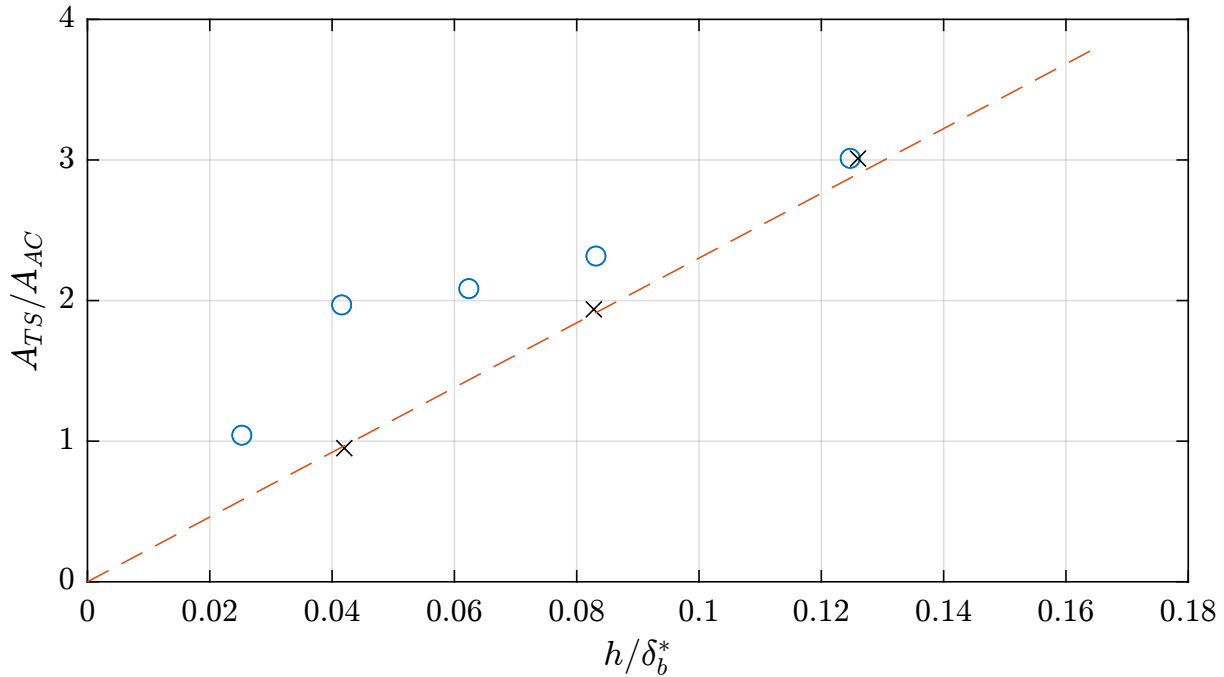
Figure 27 – Maximum of the TS amplitude from acoustic receptivity of gaps at $X^*/\delta_b^* = 1108.8$ divided by the freestream acoustic wave amplitude. Comparison among the experimental data of Placidi et al. (2020) (circles), the linearised simulation data present in Placidi's paper (dashed line), and the present DNS simulation (cross). The present simulation was correct to match the lowest height from the experiment.
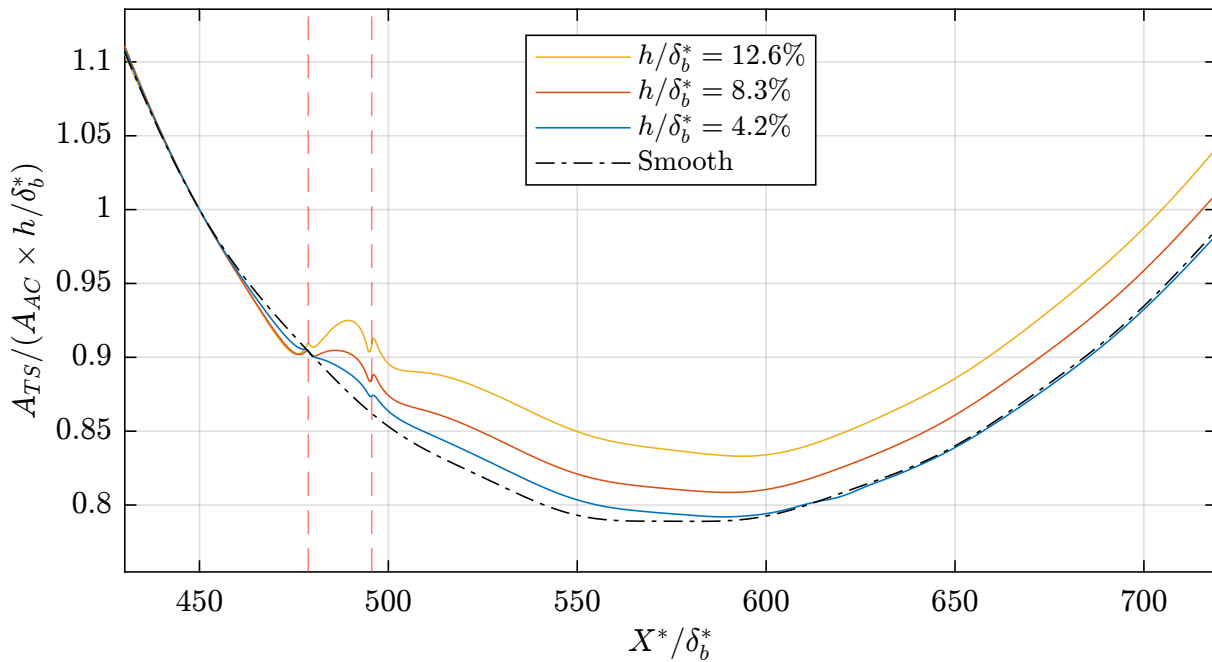
Figure 28 – Amplitude of TS waves passing over the smooth surface and rough surface with a localized rectangular gap.
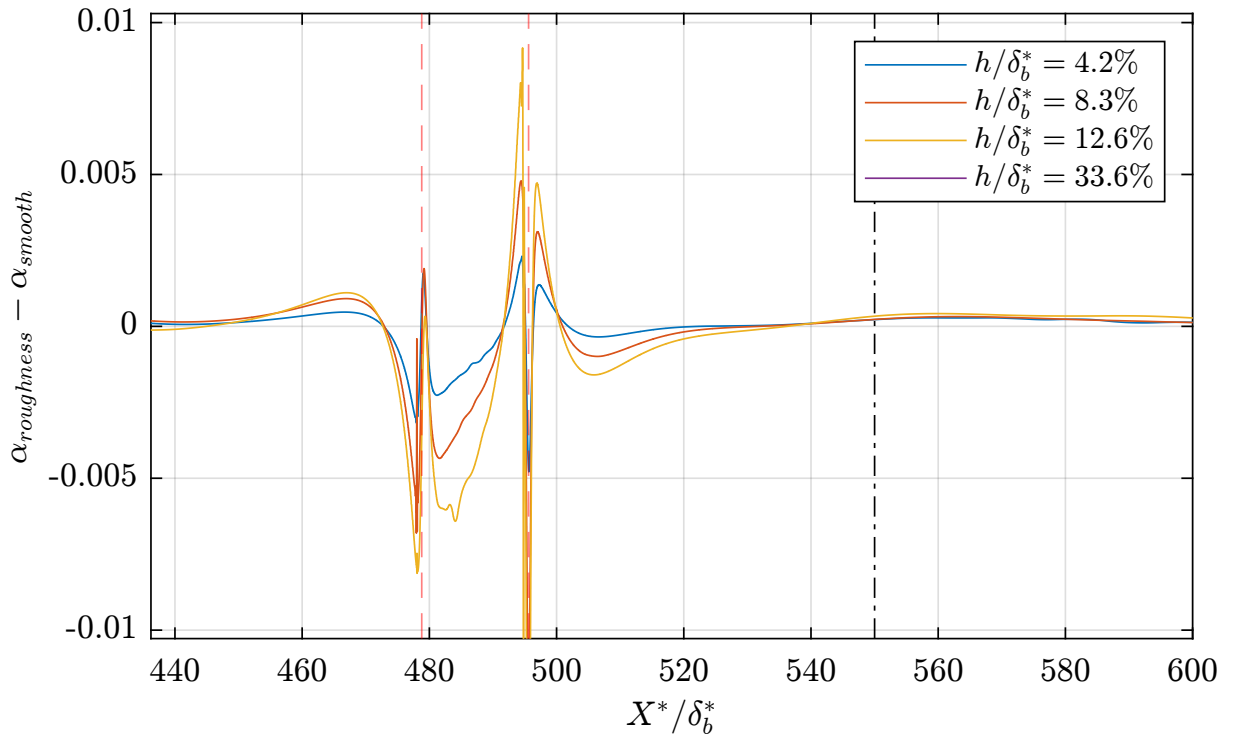
Figure 29 – Disturbance in the growth rate (α) between the cases with and without cavity.
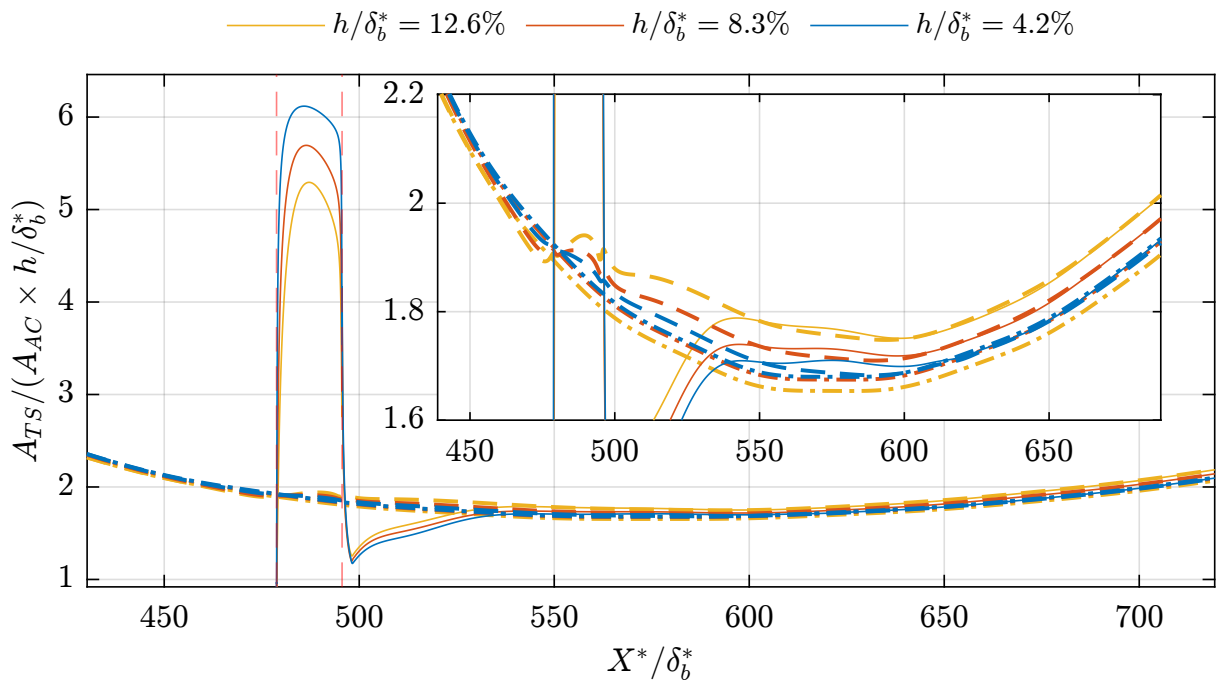
Figure 30 – Comparison among the maximum of the TS amplitude generated by acoustic receptivity for different cavity depths normalized by the acoustic wave amplitude and the cavity depth (solid lines). This figure also presents the normalized maximum amplitude of the TS passing over the cavity (dashed) and the normalized maximum amplitude of the TS passing over the smooth plate (dash-dotted).
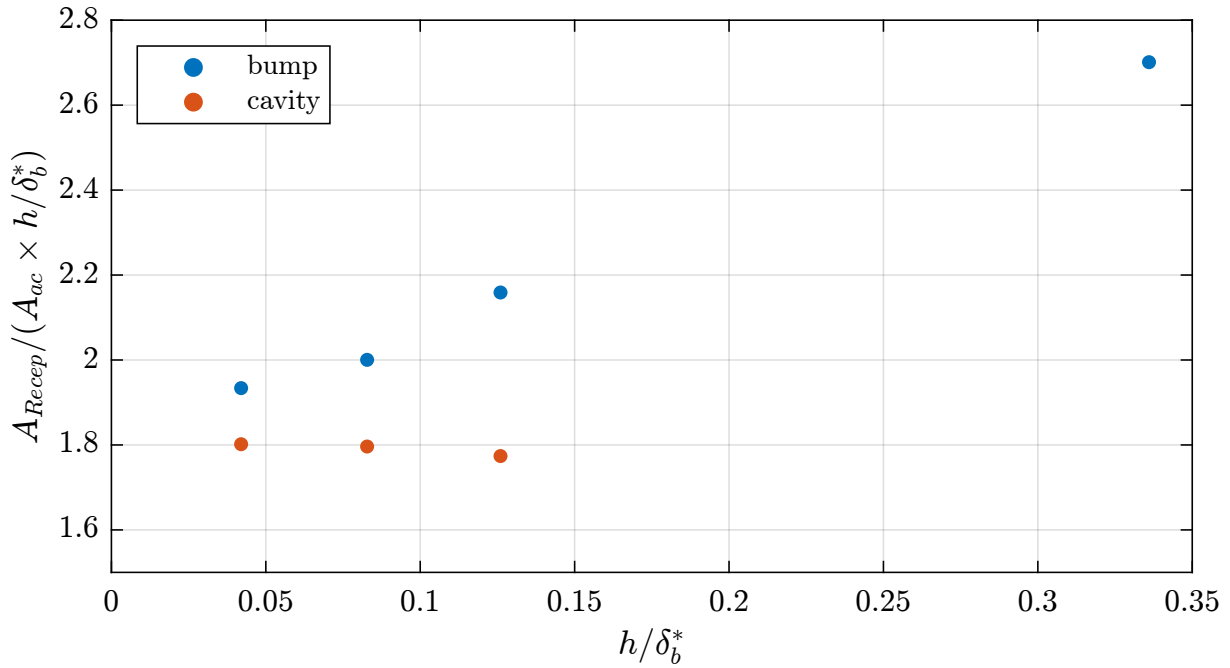
Figure 31 – Receptivity coefficient at the center of the roughness for different cavity and bump heights. The amplitudes were measured with the procedure described in section 5.1.
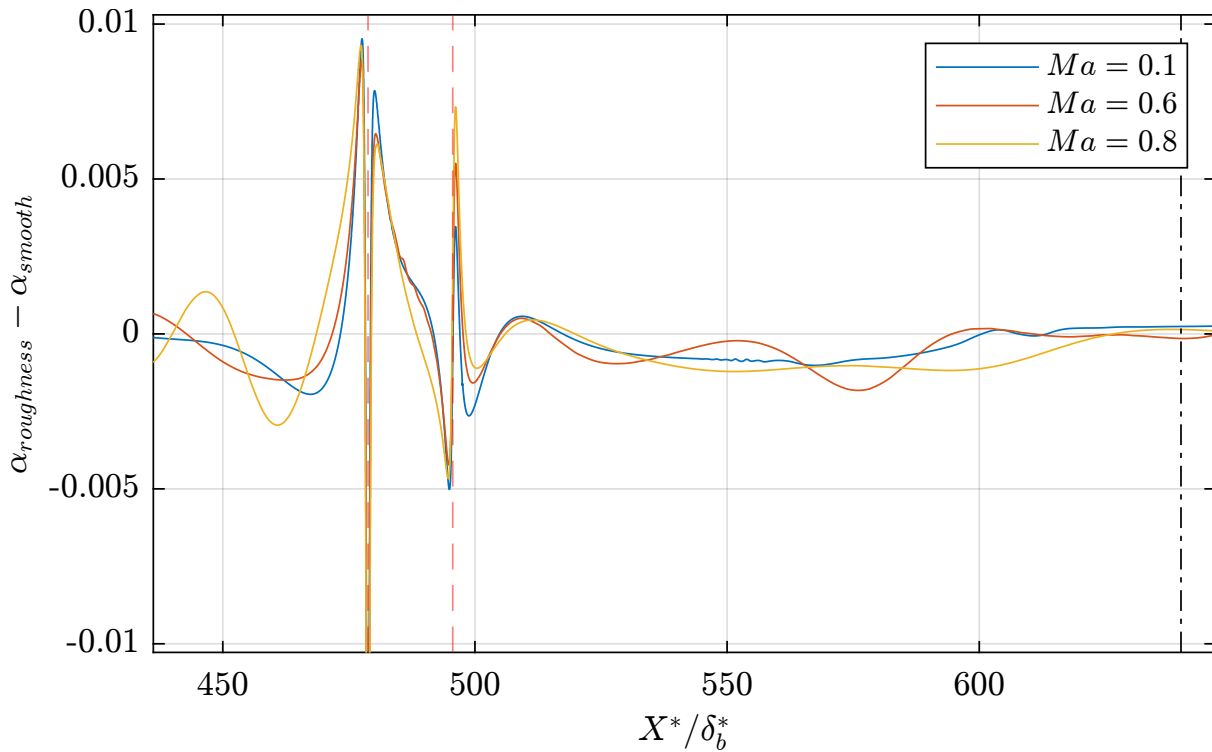
Figure 32 – Disturbance in the growth rate (α) between the cases with different Mach numbers. The disturbance in each case is from the bump with $h/\delta_b^* = 12.6\%$.
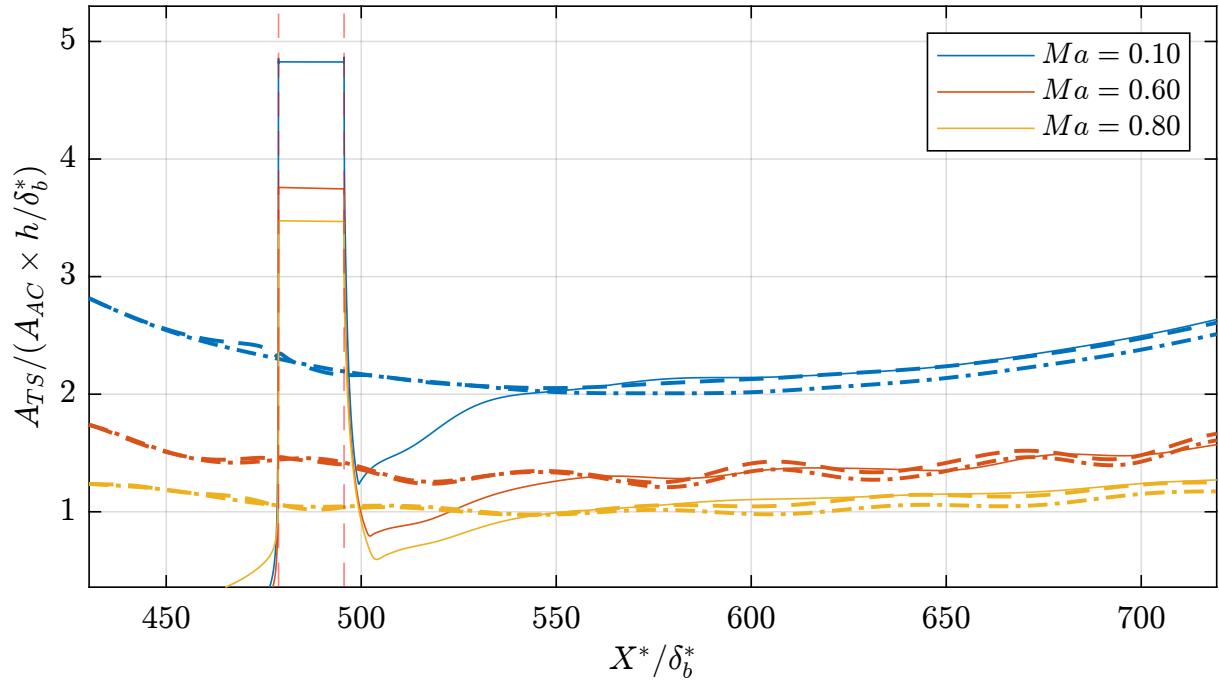
Figure 33 – TS amplitude over the flat plate (maximum in the vertical direction) for different Mach numbers.

Figure 34 – Receptivity coefficient at the center of the roughness for different Mach numbers. The amplitudes were measured with the procedure described in section 5.1.

7 CONCLUSION

This work studies the physics of the receptivity of TS waves to acoustic waves in the laminar boundary layer. The method utilized was Direct Numerical Simulation with high-order compact finite differences and body-fitting mesh. This study covered the receptivity to small rectangular positive or negative elements (bump or gap, respectively) and the Mach number effect.
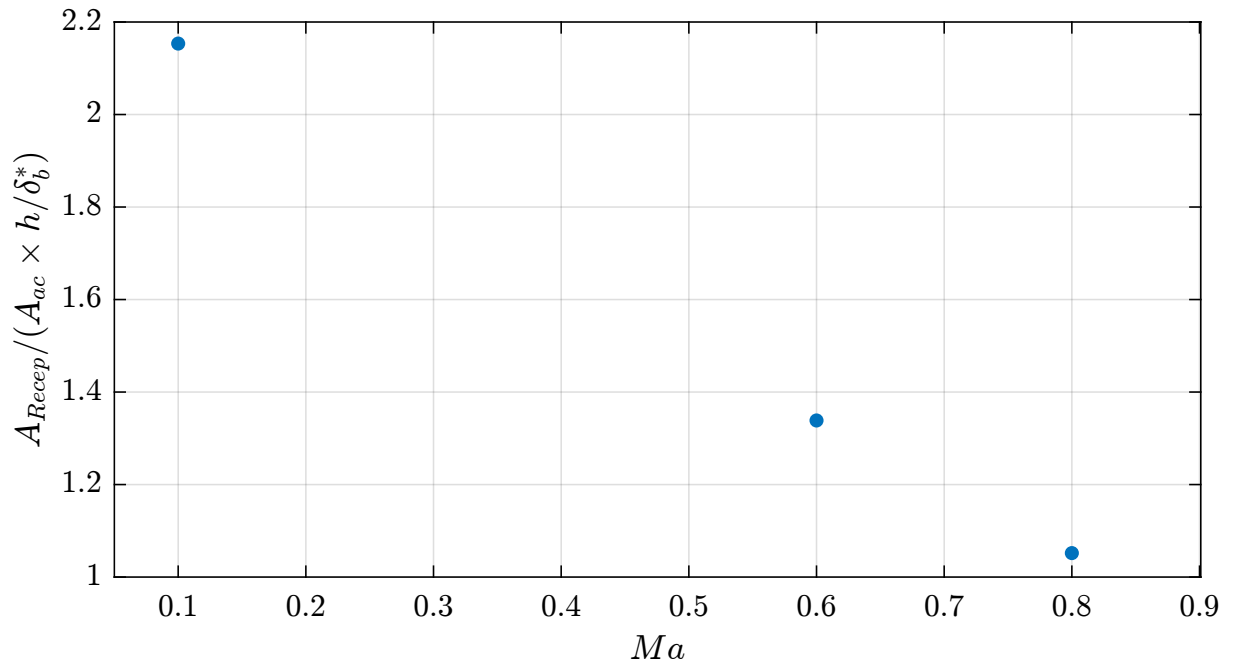
A more robust way to measure receptivity was suggested, and the comparison with the simulation data from the literature also suggests that this procedure leads to more reliable values of receptivity. After the validation, the experimental data were compared, and the possible implications of the pressure gradient in the evolution of the TS wave were evaluated as a possible explanation for the differences encountered.

The results showed in this paper suggested that the receptivity of the bump starts the non-linear regime in heights greater than 4.2% of δ_b^*. Moreover, the receptivity of cavities seemed to be smaller than the receptivity of bumps, which was not predicted by the linearised theories, such as the Finite Reynolds Number Theory of Choudhari and Streett (1992). At last, the results show that the receptivity decreases with the Mach number, and this trend appears to agree with Raposo, Mughal and Ashworth (2019).

The present work presented a remarkable agreement with the literature data within the linear regime; the results spotted the limit of the linear and non-linear regimes. For future works, a suggestion might be the study of the interference of different frequencies co-occurring and the three-dimensional non-linear receptivity. In addition, the study of deeper gaps is also worth assessing its non-linearity.

REFERENCES

ÅKERVIK, E. *et al.* Steady solutions of the Navier-Stokes equations by selective frequency damping. **Physics of Fluids**, 2006. ISSN 10706631.

BERGAMO, L. F. Instabilidade hidrodinâmica linear do escoamento compressível em uma cavidade. Biblioteca Digital de Teses e Dissertações da Universidade de São Paulo, São Carlos, apr 2014. Available at: http://www.teses.usp.br/teses/disponiveis/18/18148/tde-28052014-164324/.

BODONYI, R. Nonlinear triple-deck studies in boundary-layer receptivity. 1990.

CHOUDHARI, M. Boundary-layer receptivity due to distributed surface imperfections of a deterministic or random nature. **Theor. Comput. Fluid Dyn.**, v. 4, n. 3, p. 101, 1993.

CHOUDHARI, M.; DUCK, P. W. Nonlinear excitation of inviscid stationary vortex instabilities in a boundary-layer flow. *In*: SPRINGER. **IUTAM Symposium on Nonlinear Instability and Transition in Three-Dimensional Boundary Layers**. [*S.l.: s.n.*], 1996. p. 409–422.

CHOUDHARI, M.; STREETT, C. L. A finite Reynolds-number approach for the prediction of boundary-layer receptivity in localized regions. **Physics of Fluids A: Fluid Dynamics**, v. 4, n. 11, p. 2495, 1992.

CROUCH, J. D. Localized receptivity of boundary layers. **Physics of Fluids A**, v. 4, n. 7, p. 1408–1414, 1992. ISSN 08998213.

DE TULLIO, N.; RUBAN, A. I. A numerical evaluation of the asymptotic theory of receptivity for subsonic compressible boundary layers. **Journal of Fluid Mechanics**, v. 771, p. 520–546, 2015. Available at: doi:10.1017/jfm.2015.196.

ERIKSSON, L. E.; RIZZI, A. Computer-aided analysis of the convergence to steady state of discrete approximations to the euler equations. **Journal of Computational Physics**, 1985. ISSN 10902716.

FOX, R. W.; PRITCHARD, P. J.; MCDONALD, A. T. **Introdução À Mecânica Dos Fluidos .** 8. ed. Rio de Janeiro, Brasil: Grupo Gen-LTC, 2014. 884 p. ISBN 852162302X.

GAITONDE, D. V.; VISBAL, M. R. High-order schemes for Navier-Stokes equations: algorithm and implementation into FDL3DI. **Air Vehicles Directorate**, 1998.

GOLDSTEIN, M. E. The evolution of Tollmien–Schlichting waves near a leading edge. **Journal of Fluid Mechanics**, Cambridge University Press, v. 127, p. 59–81, 1983.

GOLDSTEIN, M. E. Scattering of acoustic waves into Tollmien-Schlichting waves by small streamwise variations in surface geometry. **Journal of Fluid Mechanics**, v. 154, p. 509–529, 1985. ISSN 14697645.

INGEN, J. van. A suggested semi-empirical method for the calculation of the boundary layer transition region. **Technische Hogeschool Delft, Vliegtuigbouwkunde, Rapport VTH-74**, Delft University of Technology, 1956. Available at: https://www.narcis.nl/publication/RecordID/oai:tudelft.nl:uuid:cff1fb47-883f-4cdc-ad07-07d264f3fd10.

KAYNAK, Ü.; EMRE, G. Boundary-layer transition under the effect of compressibility for the correlation Based Transition Model. *In*: **46th AIAA Aerospace Sciences Meeting and Exhibit**. [*S.l.: s.n.*], 2008. ISBN 9781563479373.

KURZ, H. B.; KLOKER, M. J. Receptivity of a swept-wing boundary layer to micron-sized discrete roughness elements. **Journal of fluid mechanics**, Cambridge University Press, v. 755, p. 62–82, 2014.

LELE, S. K. Compact finite difference schemes with spectral-like resolution. **Journal of Computational Physics**, 1992. ISSN 10902716.

LI, N.; LAIZET, S. 2DECOMP & FFT-A Highly Scalable 2D Decomposition Library and FFT Interface. **Cray User Group 2010 conference**, 2010.

MAREC, J. P. Drag Reduction: a Major Task for Research. *In*: **Aerodynamic Drag Reduction Technologies**. [*S.l.: s.n.*], 2001.

MARTINEZ, G. A. G.; MEDEIROS, M. A. F. Direct numerical simulation of a wavepacket in a boundary layer at Mach 0.9. *In*: **46th AIAA Fluid Dynamics Conference**. Reston, Virginia: American Institute of Aeronautics and Astronautics, 2016. ISBN 978-1-62410-436-7. Available at: http://arc.aiaa.org/doi/10.2514/6.2016-3195.

MATHIAS, M. S.; MEDEIROS, M. A. F. Direct Numerical Simulation of a Compressible Flow and Matrix-Free Analysis of its Instabilities over an Open Cavity. **Journal of Aerospace Technology and Management**, Departamento de Ciência e Tecnologia Aeroespacial, v. 10, jul 2018. ISSN 2175-9146. Available at: http://www.jatm.com.br/ojs/index.php/jatm/article/view/949.

MONSCHKE, J. A.; KUESTER, M. S.; WHITE, E. B. Acoustic receptivity measurements using modal decomposition of a modified orr–sommerfeld equation. **AIAA Journal**, American Institute of Aeronautics and Astronautics, v. 54, n. 3, p. 805–815, 2016.

MORKOVIN, M. V. On the many faces of transition. *In*: **Viscous drag reduction**. [*S.l.: s.n.*]: Springer, 1969. p. 1–31.

MORKOVIN, M. V. Transition in open flow systems-a reassessment. **Bull. Am. Phys. Soc.**, v. 39, p. 1882, 1994.

NAYFEH, A. H.; ASHOUR, O. N. Acoustic receptivity of a boundary layer to Tollmien–Schlichting waves resulting from a finite-height hump at finite Reynolds numbers. **Phys. Fluids**, v. 6, n. 11, p. 3705, 1994.

PLACIDI, M.; GASTER, M.; ATKIN, C. J. Acoustic excitation of Tollmien-Schlichting waves due to localised surface roughness. **Journal of Fluid Mechanics**, p. 1–13, 2020. ISSN 14697645.

PRANDTL, L. Motion of fluids with very little viscosity. **HOUILLE BLANCE**, p. 75–82, mar 1904. Available at: https://ntrs.nasa.gov/search.jsp?R=19930090813.

RAPOSO, H.; MUGHAL, S. M.; ASHWORTH, R. Acoustic receptivity and transition modeling of Tollmien-Schlichting disturbances induced by distributed surface roughness. **Physics of Fluids**, American Institute of Physics, v. 30, n. 4, p. 44105, apr 2018. ISSN 1070-6631. Available at: https://doi.org/10.1063/1.5024909.

RAPOSO, H.; MUGHAL, S. M.; ASHWORTH, R. An adjoint compressible linearised Navier-Stokes approach to model generation of Tollmien-Schlichting waves by sound. **Journal of Fluid Mechanics**, v. 877, p. 105–129, 2019. ISSN 14697645.

RAYLEIGH, L. On the Stability, or Instability, of certain Fluid Motions. **Proceedings of the London Mathematical Society**, Oxford University Press (OUP), s1-11, n. 1, p. 57–72, nov 1879. ISSN 00246115. Available at: http://doi.wiley.com/10.1112/plms/s1-11.1.57.

REED, H. L.; SARIC, W. S.; ARNAL, D. Linear Stability Theory. **Annual Review of Fluid Mechanics**, v. 28, p. 389–428, 1996.

RENEAUX, J. Overview on drag reduction technologies for civil transport aircraft. *In*: **ECCOMAS 2004 - European Congress on Computational Methods in Applied Sciences and Engineering**. [*S.l.: s.n.*], 2004.

REYNOLDS, O. An Experimental Investigation of the Circumstances Which Determine Whether the Motion of Water Shall Be Direct or Sinuous , and of the Law of Resistance in Parallel Channels . [Abstract] Author (s): Osborne Reynolds Source : Proceedings of the Royal S. **Philosophical Transactions of the Royal Society of London**, v. 35, n. 1883, p. 84–99, 1883. ISSN 0261-0523.

RUBAN, A. On the generation of Tollmien-Schlichting waves by sound. **Fluid Dynamics**, v. 19, n. 5, p. 709–717, 1984.

SARIC, W. S. Physical description of boundary-layer transition: Experimental evidence. **In AGARD**, 1994.

SARIC, W. S.; REED, H. L.; KERSCHEN, E. J. Boundary-Layer Receptivity to Freenstream Disturbances. **Annual Review of Fluid Mechanics**, Annual Reviews, v. 34, n. 1, p. 291–319, jan 2002. ISSN 0066-4189.

SARIC, W. S.; WHITE, E. B. Influence of high-amplitude noise on boundary-layer transition to turbulence. *In*: **29th AIAA Fluid Dynamics Conference**. [*S.l.: s.n.*], 1998. p. 1–11.

SMITH, A. M. O. Transition, pressure gradient and stability theory. **Douglas Aircraft Co., Report ES 26388**, 1956.

TEMPERTON, C. Algorithms for the solution of cyclic tridiagonal systems. **Journal of Computational Physics**, Elsevier, v. 19, n. 3, p. 317–323, 1975.

VEERASAMY, D. **Effect on flap transition of upstream wake turbulence**. 2019. Tese (Doutorado) — City, University of London, 2019.

WHITE, F. M.; CORFIELD, I. **Viscous fluid flow**. 3. ed. [*S.l.: s.n.*]: McGraw-Hill New York, 2006. v. 1. ISBN 0-07-069712-4.

WÖRNER, A.; RIST, U.; WAGNER, S. Humps/steps influence on stability characteristics of two-dimensional laminar boundary layer. **AIAA Journal**, v. 41, n. 2, p. 192–197, feb 2003. ISSN 00011452. Available at: http://arc.aiaa.org/doi/10.2514/2.1960.

WÜRZ, W. *et al.* Three-dimensional acoustic-roughness receptivity of a boundary layer on an airfoil: Experiment and direct numerical simulations. **Journal of Fluid Mechanics**, v. 478, n. 478, p. 135–163, 2003. ISSN 00221120.

WÜRZ, W. *et al.* Three-dimensional acoustic-roughness receptivity of a boundary layer on an airfoil: experiment and direct numerical simulations. **Journal Of Fluid Mechanics**, v. 478, n. 478, p. 135–163, mar 2003. ISSN 0022-1120.